

國立交通大學

電子工程學系 電子研究所碩士班

碩士論文

電子穿越氮化銦及氮化鈦表面的
非彈性交互作用之研究



**Inelastic Interactions of Elections
Crossing the Surface of
Indium Nitride and Titanium Nitride**

研究生：姜崇勝

指導教授：桂正楣

中華民國九十七年六月

電子穿越氮化銦及氮化鈦表面的
非彈性交互作用之研究

**Inelastic Interactions of Elections Crossing the
Surface of Indium Nitride and Titanium Nitride**

研究生：姜崇勝

Student: Chung-Sheng Chiang

指導教授：桂正楣

Advisor: Cheng-May Kwei

國立交通大學
電子工程學系電子研究所

碩士論文



A Thesis

Submitted to

**Department of Electronics Engineering & Institute of Electronics
College of Electrical and Computer Engineering
National Chiao Tung University
In Partial Fulfillment of the Requirements
For the Degree of
Master
In
Electronics Engineering**

June 2008

Hsinchu, Taiwan, Republic of China

中華民國九十七年六月

電子穿越氮化銦及氮化鈦表面的 非彈性交互作用之研究

研究生：姜崇勝

指導教授：桂正楣

國立交通大學

電子工程學系電子研究所碩士班



本論文根據電磁介電理論來研究電子穿越氮化銦及氮化鈦表面時，電子與固體間發生之非彈性交互作用。體激發效應及表面激發效應都對非彈性散射截面有所貢獻。在介電理論中，相關的激發效應可以用介電函式來描述，本論文利用實驗所量測到的光學數據來決定延伸式德魯特函式介電中的參數。接著計算入射或出射電子的微分倒數非彈性平均自由行徑及倒數非彈性平均自由行徑，並分析當電子以不同的電子能量、穿越角度、或離穿越點不同距離穿越氮化銦及氮化鈦表面時對微分倒數非彈性平均自由行徑及倒數非彈性平均自由行徑的影響。電子在固體外移動所產生激發的總機率可以用表面激發參數來詮釋，本研究也將計算電子入射或出射氮化銦及氮化鈦表面造成的表面激發參數，並分析當電子以不同的

電子能量或不同穿越角度入射或出射氮化銦及氮化鈦表面時對表面激發參數的影響。



Inelastic Interactions of Electrons Crossing the Surface of Indium Nitride and Titanium Nitride

Student : Chung-Sheng Chiang

Advisor : Cheng-May Kwei

Department of Electronics Engineering and

Institute of Electronics

National Chiao Tung University



ABSTRACT

A dielectric response theory was used to study the inelastic cross sections for electrons crossing the indium nitride and titanium nitride surface. The inelastic cross sections contain information on both the surface and volume excitations. Parameters in the extended Drude dielectric function were determined from the fits of this function to experimental optical data. Theoretical derivations of the differential inverse inelastic mean free path (DIIMFP) and inverse inelastic mean free path (inverse IMFP) for either incident or escaping electrons were made for different

electron energies, crossing angles, and electron distances relative to the crossing point at the surface. Dependences of the calculated DIIMFP and inverse IMFP on electron energy, crossing angle, and electron distance were analyzed. Surface excitation parameter (SEP), which describes the total probability of the surface excitations for the electrons moving outside the solid, was also calculated for different electron energies and crossing angles. The energy and angular dependences of the calculated SEPs were also analyzed.



ACKNOWLEDGEMENTS

I would like to express my sincere gratitude to my thesis advisor, Prof. C. M. Kwei, for her guidance and encouragement during the course of the work. I would also like to appreciate my senior, Y. H. Tu, for his invaluable comments and suggestions. In addition, special thanks are given to the previous and present members working in Solid State Physics Development Laboratory for their helpful discussion and assistance.

This thesis is dedicated to my family for their love.



CONTENTS

ABSTARCT (CHINESE)	i
ABSTARCT (ENGLISH)	iii
ACKNOWLEDGEMENTS	v
CONTENTS	vi
TABLE CAPTIONS	viii
FIGURE CAPTIONS	ix
CHAPTER 1 INTRODUCTION	1
CHAPTER 2 DIELECTRIC RESPONSE THEORY	4
2.1 Extended Drude Dielectric Function	4
2.2 Induced Potential	9
2.3 Differential Inverse Inelastic Mean Free Path	13
2.4 Surface Excitation Parameter	15
CHAPTER 3 RESULTS AND DISCUSSION	18
3.1 Parameters of Extended Drude Dielectric Function	18
3.2 Dielectric Function and Energy Loss Function	18

3.3	Differential Inverse Inelastic Mean Free Path	19
3.4	Inverse Inelastic Mean Free Path	21
3.5	Surface Excitation Parameter	23
CHAPTER 4 CONCLUSIONS		26
REFERENCES		28
TABLE		31
FIGURE		33
VITA		54



Table Captions

Table 3.1 Parameters in the dielectric function of Eq. (2.6) for InN and TiN. 31

Table 3.2 Fitted values of parameters a , b and c in Eq. (2.29) for InN and 32
TiN.



Figure Captions

Fig. 2.1 A plot of the problem studied in this work. An electron of charge e^- and velocity \vec{v} moves across the interface at time $t = 0$ from medium 1 to medium 2 with crossing angle α . $\epsilon_1(q, \omega)$ and $\epsilon_2(q, \omega)$ are, respectively, dielectric functions of the media 1 and 2. The instant position of the electron is $\vec{r} = \vec{v}t$, relative to the crossing point at the interface. 33

Fig. 3.1 A plot of the real and imaginary parts of the dielectric function, $\epsilon_R(0, \omega)$ and $\epsilon_I(0, \omega)$, and the volume and surface loss functions, $\text{Im}[-1/\epsilon(0, \omega)]$ and $\text{Im}[-1/(\epsilon(0, \omega)+1)]$, for InN. Solid and dotted curves are, respectively, calculated results of the present work and experimental data [14, 15]. 34

Fig. 3.2 A plot of the real and imaginary parts of the dielectric function, $\epsilon_R(0, \omega)$ and $\epsilon_I(0, \omega)$, and the volume and surface loss functions, $\text{Im}[-1/\epsilon(0, \omega)]$ and $\text{Im}[-1/(\epsilon(0, \omega)+1)]$, for TiN. Solid and dotted curves are, respectively, calculated results of the present work and experimental data [16]. 35

- Fig. 3.3** Calculated results of the DIIMFP for a 500 eV electron escaping 36
from InN to vacuum with different crossing angles and distances
from the crossing point at the surface, either outside ($r > 0$) or
inside ($r < 0$) the solid.
- Fig. 3.4** Calculated results of the DIIMFP for a 500 eV electron incident 37
from vacuum to InN with different crossing angles and distances
from the crossing point at the surface, either outside ($r < 0$) or
inside ($r > 0$) the solid.
- Fig. 3.5** Calculated results of the DIIMFP for a 500 eV electron escaping 38
from TiN to vacuum with different crossing angles and distances
from the crossing point at the surface, either outside ($r > 0$) or
inside ($r < 0$) the solid.
- Fig. 3.6** Calculated results of the DIIMFP for a 500 eV electron incident 39
from vacuum to TiN with different crossing angles and distances
from the crossing point at the surface, either outside ($r < 0$) or
inside ($r > 0$) the solid.
- Fig. 3.7** Calculated results of the DIIMFP for a 60° crossing angle electron 40
escaping from InN to vacuum for several electron energies with
different distances from the crossing point at the surface, either
outside ($r > 0$) or inside ($r < 0$) the solid.

- Fig. 3.8** Calculated results of the DIIMFP for a 60° crossing angle electron 41
incident from vacuum to TiN for several electron energies with
different distances from the crossing point at the surface, either
outside ($r < 0$) or inside ($r > 0$) the solid.
- Fig. 3.9** A plot of the inverse IMFP for a 500 eV electron escaping from InN 42
to vacuum with different crossing angles as a function of electron
distance from the crossing point at the surface, either outside
($r > 0$) or inside ($r < 0$) the solid.
- Fig. 3.10** A plot of the inverse IMFP for a 500 eV electron incident from 43
vacuum to InN with different crossing angles as a function of
electron distance from the crossing point at the surface, either
outside ($r < 0$) or inside ($r > 0$) the solid.
- Fig. 3.11** A plot of the inverse IMFP for a 500 eV electron escaping from TiN 44
to vacuum with different crossing angles as a function of electron
distance from the crossing point at the surface, either outside
($r > 0$) or inside ($r < 0$) the solid.
- Fig. 3.12** A plot of the inverse IMFP for a 500 eV electron incident from 45
vacuum to TiN with different crossing angles as a function of
electron distance from the crossing point at the surface, either
outside ($r < 0$) or inside ($r > 0$) the solid.

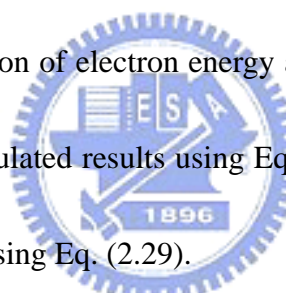
- Fig. 3.13** A plot of the inverse IMFP for a 60° crossing angle electron 46
 escaping from InN to vacuum with different electron energies as a
 function of electron distance from the crossing point at the surface,
 either outside ($r > 0$) or inside ($r < 0$) the solid.
- Fig. 3.14** A plot of the inverse IMFP for a 60° crossing angle electron 47
 incident from vacuum to TiN with different electron energies as a
 function of electron distance from the crossing point at the surface,
 either outside ($r < 0$) or inside ($r > 0$) the solid.
- Fig. 3.15** A plot of the SEP for escaping electrons moving from InN to 48
 vacuum as a function of electron energy and crossing angle. Solid
 circles are the calculated results using Eq. (2.27). Solid curves are
 the fitting results using Eq. (2.29). 
- Fig. 3.16** A plot of the SEP for incident electrons moving from vacuum to InN 49
 as a function of electron energy and crossing angle. Solid circles
 are the calculated results using Eq. (2.28). Solid curves are the
 fitting results using Eq. (2.29).
- Fig. 3.17** A plot of the SEP for escaping electrons moving from TiN to 50
 vacuum as a function of electron energy and crossing angle. Solid
 circles are the calculated results using Eq. (2.27). Solid curves are
 the fitting results using Eq. (2.29).

Fig. 3.18 A plot of the SEP for incident electrons moving from vacuum to TiN 51

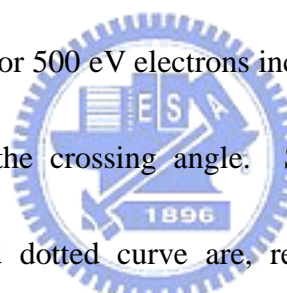
as a function of electron energy and crossing angle. Solid circles are the calculated results using Eq. (2.28). Solid curves are the fitting results using Eq. (2.29).

Fig. 3.19 A plot of the SEP for 500 eV electrons escaping from InN to 52

vacuum as a function of the crossing angle. Solid circles, solid curve, dashed curve, and dotted curve are, respectively, the calculated result using Eq. (2.27), the fitting results using Eq. (2.29), the previous model [5], and the Oswald's model [17].

Fig. 3.20 A plot of the SEP for 500 eV electrons incident from vacuum to TiN 53

as a function of the crossing angle. Solid circles, solid curve, dashed curve, and dotted curve are, respectively, the calculated result using Eq. (2.28), the fitting results using Eq. (2.29), the previous model [5], and the Oswald's model [17].



CHAPTER 1

INTRODUCTION

In the rapid development of nano-science, the study of surface phenomenon plays a crucial role because of the increasing surface-to-volume ratio. Many electron spectroscopies, such as the Auger electron spectroscopy (AES), x-ray photoelectron spectroscopy (XPS) and reflection electron energy loss spectroscopy (REELS), are sensitive to the surface layer within nanometer distance below the solid surface. Quantitative information on inelastic interaction cross sections of low-energy electrons crossing solid surfaces is important in those surface sensitive spectroscopies. Previous studies revealed that surface excitations contributed significantly to the energy-loss spectra of electrons backscattered from solid surface [1-3]. Therefore, surface excitations should be included in the analyses of electron spectroscopies.

The inelastic cross sections contain the combined effects arisen from volume and surface plasmon excitations. For electrons traveling inside the solid, the increase in surface excitations as electrons move closer to the surface is roughly compensated by the decrease in volume excitations. Therefore, the inelastic cross sections derived for an infinite solid could be applied as a good approximation in this region [4, 5].

As electrons move outside the solid, only surface excitations are possible over an effective region near to the surface. Many theoretical approaches [2, 3, 6] to surface excitations were dealt with the dielectric response theory. Such surface excitations were usually characterized by the so-called surface excitation parameter (SEP), which describes the total probability of the surface excitations for the electrons moving outside the solid [5].

Previously, Kwei et al. [5] developed an inelastic-scattering model. Kwei et al. used the dielectric response theory and solved the Poisson's equation in Fourier space by matching the boundary conditions. This model was used to calculate the SEP for normally incident and escaping electrons moving only in vacuum. For other tilted crossing angle, α , the SEP was approximated by multiplying the SEP for normally crossing angle with $(\cos\alpha)^{-1}$ [5, 7]. However, the conservations of energy and momentum were not completely satisfied because of the use of cylindrical coordinates that carried no restriction on the normal component of momentum transfer [8, 9]. Recently, Li et al. [8, 9] developed a new interaction model for obliquely incident and escaping electrons with arbitrary crossing angles. In this model, spherical coordinates were employed for momentum transfer and thus satisfied the energy and momentum conservations. In the present work, the Li's model was applied to calculate the differential inverse inelastic mean free path (DIIMFP), the

inelastic mean free path (IMFP) and surface excitation parameter (SEP) for obliquely incident and escaping electrons crossing the surface of indium nitride (InN) and titanium nitride (TiN). InN, a III-V semiconductor, is of interest for application in semiconductor devices such as lasers, light-emitting diodes, and high efficiency solar cells [10, 11]. TiN, a ceramic material, is generally used as a coating due to its outstanding properties such as high hardness, excellent corrosion resistance, chemical stability, etc [12, 13]. These calculations were performed based on the dielectric response theory using an extended Drude dielectric function with parameters obtained from a fit of this function to the experimental optical data [14-16]. Because of the strong overlapping of oscillator strengths between electrons in the valence band and the outermost inner shell, the data was fitted to include the contribution from also the outermost inner shell. Sum rules were thus employed to confirm the accuracy of these parameters. The presently calculated results were compared with corresponding data of other works [5, 17]. Dependences of the presently calculated DIIMFP and inverse IMFP on electron distance, crossing angle, and electron energy were analyzed. The angular and energy dependences of the presently calculated SEP were also analyzed. The calculated SEP was fitted to a simple formula as a function of electron energy and crossing angle.

CHAPTER 2

DIELECTRIC RESPONSE THEORY

When an electron moves across the solid surface, it may induce volume and surface excitations because of the electron-solid interactions. Volume excitations, including volume plasmon generations and inter-band transitions, arise when an electron travels deep inside the solid. Surface excitations, on the other hand, occur as an electron moves close to the interface. Both excitations can be described by the dielectric function of the solid. Recently, a modified inelastic-scattering model was developed [4, 5]. This model was performed based on the dielectric response theory using the dielectric function. By solving Poisson equations in the Fourier space and applying the boundary conditions, induced potential can be calculated. Then, the differential inverse inelastic mean free path (DIIMFP), inelastic mean free path (IMFP) and surface excitation parameter (SEP) were also calculated. Note that all quantities are expressed in atomic units (a.u.) unless otherwise specified.

2.1 Extended Drude Dielectric Function

The Drude model works fairly well for the conduction band of a free-electron-

like metal [18]. The conduction electrons are described by a free-electron gas constrained by the Fermi-Dirac statistics in this model. The Drude dielectric function in the optical limit, i.e. $q \rightarrow 0$, is given by

$$\varepsilon(0, \omega) = \varepsilon_R(0, \omega) + i\varepsilon_I(0, \omega) \quad (2.1)$$

where q is the momentum transfer, and ω is the energy transfer. For a solid having a complex structure, the valence band may be composed of several subbands.

Each i th subband is characterized by its own oscillator strength, A_i , damping constant, γ_i , and critical-point energy, ω_i . Interband transitions can be incorporated into the Drude model by adding these subband electrons to free-electron system. The imaginary part of the extended Drude dielectric function in the optical

limit, $\varepsilon_I(0, \omega)$, is given by [19]

$$\varepsilon_I(0, \omega) = \sum_i \frac{A_i \gamma_i \omega}{(\omega^2 - \omega_i^2)^2 + \omega^2 \gamma_i^2} \quad (2.2)$$

and the real part of the extended Drude dielectric function, $\varepsilon_R(0, \omega)$, is given by

$$\varepsilon_R(0, \omega) = \varepsilon_B - \sum_i \frac{A_i (\omega^2 - \omega_i^2)}{(\omega^2 - \omega_i^2)^2 + \omega^2 \gamma_i^2} \quad (2.3)$$

where A_i , γ_i and ω_i are all associated with the i -th group electrons in the valance band and, sometimes, the outermost inner shells. The background dielectric constant, ϵ_B , accounts for influence of polarizable ion cores [20].

To extend the dielectric function into the $q \neq 0$ region of the $q - \omega$ plane, we replace ω_i in Eq. (2.2) and Eq. (2.3) by $\omega_i + \frac{q^2}{2}$ [21, 22]. This extension leads to a correct behavior of the dispersion relation at the optical limit, i.e. $q \rightarrow 0$. Thus, these two equations become

$$\epsilon_1(q, \omega) = \sum_i \frac{A_i \gamma_i \omega}{(\omega^2 - (\omega_i + \frac{q^2}{2})^2)^2 + (\omega \gamma_i)^2} \quad (2.4)$$

and

$$\epsilon_R(q, \omega) = \epsilon_B - \sum_i \frac{A_i (\omega^2 - (\omega_i + \frac{q^2}{2})^2)}{(\omega^2 - (\omega_i + \frac{q^2}{2})^2)^2 + (\omega \gamma_i)^2}, \quad (2.5)$$

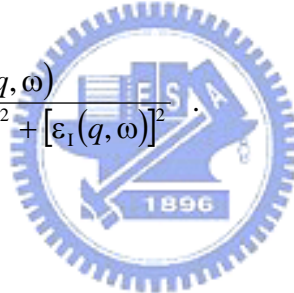
respectively. Consequently, the extended Drude dielectric function can be written as

$$\epsilon(q, \omega) = \epsilon_R(q, \omega) + i\epsilon_1(q, \omega) = \epsilon_B - \sum_i \frac{A_i}{\omega^2 - (\omega_i + \frac{q^2}{2})^2 + i\omega \gamma_i}. \quad (2.6)$$

The volume energy-loss function, or the imaginary part of the volume response function, may then be calculated from

$$\text{Im}\left[\frac{-1}{\varepsilon(q, \omega)}\right] = \frac{\varepsilon_I(q, \omega)}{[\varepsilon_R(q, \omega)]^2 + [\varepsilon_I(q, \omega)]^2} \quad (2.7)$$

Similarly, the surface energy-loss function, or the imaginary part of the surface response function, can be calculated from

$$\text{Im}\left[\frac{-1}{\varepsilon(q, \omega) + 1}\right] = \frac{\varepsilon_I(q, \omega)}{[\varepsilon_R(q, \omega) + 1]^2 + [\varepsilon_I(q, \omega)]^2} \quad (2.8)$$


In order to obtain the full spectrum of the dielectric function, the experimental optical data are frequently used [21, 23, 24]. The information of the optical data is useful for obtaining the dielectric function due to

$$\varepsilon_R(0, \omega) = n^2(\omega) - \kappa^2(\omega) \quad (2.9)$$

and

$$\varepsilon_1(0, \omega) = 2n(\omega)\kappa(\omega) \quad (2.10)$$

where $n(\omega)$ is the refraction index, and $\kappa(\omega)$ is the extinction coefficient. Therefore, all parameters (ε_B , A_i , γ_i and ω_i) of the extended Drude dielectric function in Eq. (2.6) can be determined by fits of $\varepsilon_R(0, \omega)$, $\varepsilon_1(0, \omega)$, $\text{Im}[-1/\varepsilon(0, \omega)]$ and $\text{Im}[-1/(\varepsilon(0, \omega)+1)]$ to the experimental optical data. Since optical data are usually available regarding the refraction index and the extinction coefficient in the limited frequency ranges, extrapolations are sometimes required [21, 23, 24].

Furthermore, in order to confirm the accuracy of fitting parameters, we also check the validity of the sum rules [25]

$$\int_0^\omega \omega' \varepsilon_2(0, \omega') d\omega' = 2\pi^2 N Z(\omega) \quad (2.11)$$

and

$$\int_0^\omega \omega' \text{Im} \left[\frac{-1}{\varepsilon(0, \omega')} \right] d\omega' = 2\pi^2 N \frac{Z'(\omega)}{\varepsilon_B^2} \quad (2.12)$$

where N is the number of molecules per volume, and $Z(\omega)$ and $Z'(\omega)$ are the corresponding effective numbers of electrons per molecule by excitation up to ω .

When ω is small, $Z(\omega)$ and $Z'(\omega)$ only include the contribution from valence electrons. As ω increases to a value approach the binding energy of the outermost inner-shell, outermost inner-shell electrons start to contribute. As ω increases to infinity, $Z(\omega)$ and $Z'(\omega)$ should saturate to Z_m , the total number of the electrons per molecule. Nevertheless, the ω region of available optical data usually covers with contributions only from the valence band and the outermost inner-shell. Therefore, Z_m cannot attain from the integration of Eqs. (2.11) and (2.12). In reality, we can set the upper limits of integration in Eqs. (2.11) and (2.12) to finite and infinite values. For the application of finite-range sum rules, we check $Z(\omega)$ and $Z'(\omega)$ at any given energy transfer. In the case of infinite-range sum rules, we check



$$\sum_i A_i = 4\pi N Z'_m \quad (2.13)$$

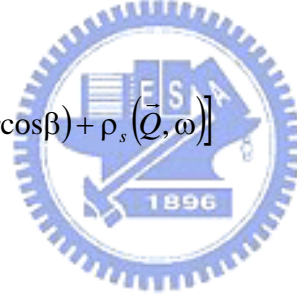
to confirm if Z'_m includes the contribution from the valence electrons and the outermost inner-shell electrons.

2.2 Induced Potential

An electron of charge e^- and velocity \vec{v} moves obliquely across the interface at time $t = 0$ from medium 1 to medium 2, as illustrated in Fig. 2.1. $\varepsilon_1(q, \omega)$ and $\varepsilon_2(q, \omega)$ are, respectively, dielectric functions of the media 1 and 2. The crossing angle α is defined as the angle between the electron moving direction and the surface normal. And $\vec{r} = \vec{v}t$ is the instant position of the electron relative to the crossing point at the interface.

The Fourier components of the scalar potential in medium 1 and medium 2 can be determined by solving the Poisson equations in the Fourier space [5, 26]; that are

$$\Phi_1(\vec{q}, \omega) = \frac{-8\pi^2}{q^2 \varepsilon_1(\vec{q}, \omega)} \left[\delta(\omega - qv \cos \beta) + \rho_s(\vec{Q}, \omega) \right] \quad (2.14)$$



for $t < 0$, and

$$\Phi_2(\vec{q}, \omega) = \frac{-8\pi^2}{q^2 \varepsilon_2(\vec{q}, \omega)} \left[\delta(\omega - qv \cos \beta) - \rho_s(\vec{Q}, \omega) \right] \quad (2.15)$$

for $t > 0$, where $\vec{q} = (\vec{Q}, q_z)$, \vec{Q} and q_z are the parallel and normal components of \vec{q} with respect to the interface, β is the angle between \vec{q} and \vec{v} , and $\rho_s(\vec{Q}, \omega)$ is the induced surface charge density. Because of the boundary condition, i.e. the continuity of the normal component of the electric displacement at the interface, the

signs in front of the $\rho_s(\vec{Q}, \omega)$ are opposite for $t < 0$ and for $t > 0$. In addition, applying the other boundary condition, i.e. the continuity of the tangential component of the electric field at the interface, the induced surface charge density can be derived as

$$\rho_s(\vec{Q}, \omega) = \frac{\int_{-\infty}^{+\infty} \frac{\delta(\omega - \vec{Q} \cdot \vec{v}_{\parallel} - q_z v_{\perp})}{q^2} \left[\frac{1}{\varepsilon_2(\vec{q}, \omega)} - \frac{1}{\varepsilon_1(\vec{q}, \omega)} \right] dq_z}{\int_{-\infty}^{+\infty} \frac{1}{q^2} \left[\frac{1}{\varepsilon_2(\vec{q}, \omega)} + \frac{1}{\varepsilon_1(\vec{q}, \omega)} \right] dq_z} \quad (2.16)$$

where v_{\parallel} and v_{\perp} are the parallel and normal components of the \vec{v} with respect to the interface. Therefore, we can obtain $\Phi_1(\vec{q}, \omega)$ and $\Phi_2(\vec{q}, \omega)$ after substituting Eq. (2.16) into Eqs. (2.14) and (2.15).

After removing the potential of the electron in the vacuum, the Fourier components of the induced potentials, $\Phi_{1,ind}(\vec{q}, \omega)$ and $\Phi_{2,ind}(\vec{q}, \omega)$, can be obtained. Then, the induced potential in the real space can be derived by applying the Fourier inverse transforms of $\Phi_{1,ind}(\vec{q}, \omega)$ and $\Phi_{2,ind}(\vec{q}, \omega)$. Adopting the spherical coordinates in the integration of momentum transfer, the induced potentials in the real space can be written as

$$\begin{aligned}\Phi_{1,ind}(\vec{r}, t) = & -\frac{1}{\pi} \iiint \delta(\omega - qv\cos\beta) \left[\frac{1}{\varepsilon_1(\vec{q}, \omega)} - 1 \right] e^{i(qv\cos\beta - \omega t)} \sin\beta d\beta dq d\omega \\ & - \frac{1}{2\pi^2} \iiint \iiint \frac{\rho_s(\vec{Q}, \omega)}{\varepsilon_1(\vec{q}, \omega)} e^{i(\vec{Q}\cdot\vec{R} - \omega t)} e^{iq_z z} \sin\theta d\phi d\theta dq d\omega\end{aligned}\quad (2.17)$$

for $t < 0$, and

$$\begin{aligned}\Phi_{2,ind}(\vec{r}, t) = & -\frac{1}{\pi} \iiint \delta(\omega - qv\cos\beta) \left[\frac{1}{\varepsilon_2(\vec{q}, \omega)} - 1 \right] e^{i(qv\cos\beta - \omega t)} \sin\beta d\beta dq d\omega \\ & + \frac{1}{2\pi^2} \iiint \iiint \frac{\rho_s(\vec{Q}, \omega)}{\varepsilon_2(\vec{q}, \omega)} e^{i(\vec{Q}\cdot\vec{R} - \omega t)} e^{iq_z z} \sin\theta d\phi d\theta dq d\omega\end{aligned}\quad (2.18)$$

for $t > 0$, where $\vec{r} = (\vec{R}, z)$, \vec{R} and z are the parallel and normal components of \vec{r} with respect to the interface. By assuming that $\varepsilon(\vec{q}, \omega) \approx \varepsilon(\vec{Q}, \omega)$ [23, 27], we can obtain

$$\frac{\rho_s(\vec{Q}, \omega)}{\varepsilon_1(\vec{q}, \omega)} = \frac{1}{\pi} \frac{Qv_{\perp}}{(\omega - \vec{Q} \cdot \vec{v}_{\parallel})^2 + Q^2 v_{\perp}^2} \frac{\varepsilon_1(\vec{Q}, \omega) - \varepsilon_2(\vec{Q}, \omega)}{\varepsilon_1(\vec{Q}, \omega) [\varepsilon_1(\vec{Q}, \omega) + \varepsilon_2(\vec{Q}, \omega)]} \quad (2.19)$$

and

$$\frac{\rho_s(\vec{Q}, \omega)}{\varepsilon_2(\vec{q}, \omega)} = \frac{1}{\pi} \frac{Qv_{\perp}}{(\omega - \vec{Q} \cdot \vec{v}_{\parallel})^2 + Q^2 v_{\perp}^2} \frac{\varepsilon_1(\vec{Q}, \omega) - \varepsilon_2(\vec{Q}, \omega)}{\varepsilon_2(\vec{Q}, \omega) [\varepsilon_1(\vec{Q}, \omega) + \varepsilon_2(\vec{Q}, \omega)]} . \quad (2.20)$$

The integrations over ω in the second integrals of Eqs. (2.17) and (2.18) can be performed by closing the contour in the upper and lower half planes for $t < 0$ and $t > 0$, respectively. In order to carry out the contour integration in the lower half plane, it is convenient to convert it into the upper half plane by replacing $e^{i(\vec{Q}\cdot\vec{R}-\omega t)}$ in Eq. (2.18) with $e^{i(\vec{Q}\cdot\vec{R}-\omega t)} = 2\cos(\omega t - \vec{Q}\cdot\vec{R}) - e^{-i(\vec{Q}\cdot\vec{R}-\omega t)}$.

2.3 Differential Inverse Inelastic Mean Free Path

The stopping power, or the stopping force, means the average energy loss per unit path length of a charged particle. The stopping power, $-\frac{dW}{ds}$, can be expressed in terms of the induced potential, $\Phi_{ind}(\vec{r}, t)$, according to [28]

$$-\frac{dW}{ds} = \frac{1}{v} \left[\frac{\partial \Phi_{ind}(\vec{r}, t)}{\partial t} \right]_{\vec{r}=\vec{v}t} . \quad (2.21)$$

Furthermore, the stopping power can be related to the differential inverse inelastic mean free path (DIIMFP), $\mu(\alpha, E, \omega, r)$, by

$$-\frac{dW}{ds} = \int_0^E \omega \mu(\alpha, E, \omega, r) d\omega \quad (2.22)$$

where E is the electron energy. For the case of an electron obliquely escaped from solid to vacuum ($s \rightarrow v$), $\varepsilon_1(q, \omega)$ and $\varepsilon_2(q, \omega)$ may be substituted for $\varepsilon(q, \omega)$ and 1, respectively. The DIIMFP is given by

$$\begin{aligned}
\mu^{s \rightarrow v}(\alpha, E, \omega, r) &= \frac{2}{\pi v^2} \int_{q_-}^{q_+} dq \frac{1}{q} \operatorname{Im} \left[\frac{-1}{\varepsilon(q, \omega)} \right] \Theta(-r) \\
&- \frac{2 \cos \alpha}{\pi^3} \int_{q_-}^{q_+} dq \int_0^{\pi/2} d\theta \int_0^{2\pi} d\phi \frac{q \sin^2 \theta \cos(q_z r \cos \alpha) \exp(-|r|Q \cos \alpha)}{\tilde{\omega}^2 + Q^2 v_{\perp}^2} \operatorname{Im} \left[\frac{-1}{\varepsilon(Q, \omega)} \right] \Theta(-r) \\
&+ \frac{4 \cos \alpha}{\pi^3} \int_{q_-}^{q_+} dq \int_0^{\pi/2} d\theta \int_0^{2\pi} d\phi \frac{q \sin^2 \theta \cos(q_z r \cos \alpha) \exp(-|r|Q \cos \alpha)}{\tilde{\omega}^2 + Q^2 v_{\perp}^2} \operatorname{Im} \left[\frac{-1}{\varepsilon(Q, \omega) + 1} \right] \Theta(-r) \\
&+ \frac{4 \cos \alpha}{\pi^3} \int_{q_-}^{q_+} dq \int_0^{\pi/2} d\theta \int_0^{2\pi} d\phi \frac{q \sin^2 \theta \exp(-|r|Q \cos \alpha)}{\tilde{\omega}^2 + Q^2 v_{\perp}^2} \operatorname{Im} \left[\frac{-1}{\varepsilon(Q, \omega) + 1} \right] \left[2 \cos \left(\frac{\tilde{\omega} r}{v} \right) - \exp(-|r|Q \cos \alpha) \right] \Theta(r)
\end{aligned} \tag{2.23}$$



A similar calculation can be performed for the case of electrons obliquely incident from vacuum to solid ($v \rightarrow s$), by replaced $\varepsilon_1(q, \omega)$ and $\varepsilon_2(q, \omega)$ with 1 and $\varepsilon(q, \omega)$. Then the DIIMFP is given by

$$\begin{aligned}
\mu^{v \rightarrow s}(\alpha, E, \omega, r) &= \frac{4 \cos \alpha}{\pi^3} \int_{q_-}^{q_+} dq \int_0^{\pi/2} d\theta \int_0^{2\pi} d\phi \frac{q \sin^2 \theta \cos(q_z r \cos \alpha) \exp(-|r|Q \cos \alpha)}{\tilde{\omega}^2 + Q^2 v_{\perp}^2} \operatorname{Im} \left[\frac{-1}{\varepsilon(Q, \omega) + 1} \right] \Theta(-r) \\
&+ \frac{2}{\pi v^2} \int_{q_-}^{q_+} dq \frac{1}{q} \operatorname{Im} \left[\frac{-1}{\varepsilon(q, \omega)} \right] \Theta(r) \\
&- \frac{2 \cos \alpha}{\pi^3} \int_{q_-}^{q_+} dq \int_0^{\pi/2} d\theta \int_0^{2\pi} d\phi \frac{q \sin^2 \theta \exp(-|r|Q \cos \alpha)}{\tilde{\omega}^2 + Q^2 v_{\perp}^2} \operatorname{Im} \left[\frac{-1}{\varepsilon(Q, \omega)} \right] \left[2 \cos \left(\frac{\tilde{\omega} r}{v} \right) - \exp(-|r|Q \cos \alpha) \right] \Theta(r) \\
&+ \frac{4 \cos \alpha}{\pi^3} \int_{q_-}^{q_+} dq \int_0^{\pi/2} d\theta \int_0^{2\pi} d\phi \frac{q \sin^2 \theta \exp(-|r|Q \cos \alpha)}{\tilde{\omega}^2 + Q^2 v_{\perp}^2} \operatorname{Im} \left[\frac{-1}{\varepsilon(Q, \omega) + 1} \right] \left[2 \cos \left(\frac{\tilde{\omega} r}{v} \right) - \exp(-|r|Q \cos \alpha) \right] \Theta(r)
\end{aligned} \tag{2.24}$$

where $Q = q\sin\theta$, $q_z = q\cos\theta$, $v_{\perp} = \sqrt{2E} \cos\alpha$, $\tilde{\omega} = \omega - qv\sin\theta\cos\phi\sin\alpha$, and $\Theta(r)$ is the Heaviside step function. The upper and lower limits of q are $q_{\pm} = \sqrt{2E} \pm \sqrt{2(E-\omega)}$, which are derived from conservations of energy and momentum. Note that terms containing $\text{Im}[-1/(\varepsilon+1)]$ are the contribution from surface excitations, whereas terms involving $\text{Im}[-1/\varepsilon]$ are the contribution from volume excitation.

2.4 Surface Excitation Parameter

When an electron moves inside a solid, surface and volume excitations are treated together by the use of a depth-independent inelastic mean free path (IMFP) due to the approximate compensation of these excitations at any given depth [5, 8].

The inverse IMFPs for obliquely escaping and incident electrons are, respectively, given by

$$\mu^{s \rightarrow v}(\alpha, E, r) = \int_0^E \mu^{s \rightarrow v}(\alpha, E, \omega, r) d\omega \quad (2.25)$$

and

$$\mu^{v \rightarrow s}(\alpha, E, r) = \int_0^E \mu^{v \rightarrow s}(\alpha, E, \omega, r) d\omega \quad . \quad (2.26)$$

Since only surface excitations are possible for an electron moving outside the solid, the surface excitation parameters (SEPs) are defined as the total probability of the surface excitations for the electrons moving in vacuum. The SEP can be calculated as the integration of the inverse IMFP over the whole path length of the electron outside the solid [5]. Thus, the SEPs for obliquely escaping and incident electrons are, respectively, given by

$$P_s^{s \rightarrow v}(\alpha, E) = \int_0^\infty \mu^{s \rightarrow v}(\alpha, E, r) dr \quad (2.27)$$



and

$$P_s^{v \rightarrow s}(\alpha, E) = \int_{-\infty}^0 \mu^{v \rightarrow s}(\alpha, E, r) dr \quad . \quad (2.28)$$

Eqs. (2.27) and (2.28) indicate that the SEP depends on electron energy and crossing angle. Examining these calculated results, we found that the SEPs generally follow a simple formula [9]

$$P_s^{s \rightarrow v}(\alpha, E) \text{ or } P_s^{v \rightarrow s}(\alpha, E) = \frac{aE^{-b}}{\cos^c \alpha} \quad (2.29)$$

where a , b and c are the fitting coefficients, which are material dependent.

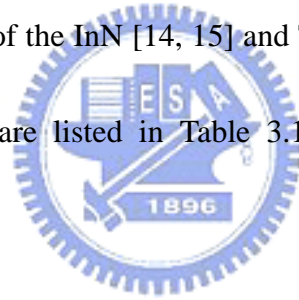


CHAPTER 3

Results and Discussion

3.1 Parameters of Extended Drude Dielectric Function

In the present work, we determined all parameters (ϵ_B , A_i , γ_i and ω_i) of the extended Drude dielectric function in Eq. (2.6) by fitting $\epsilon_R(0, \omega)$, $\epsilon_I(0, \omega)$, $\text{Im}[-1/\epsilon(0, \omega)]$ and $\text{Im}[-1/(\epsilon(0, \omega)+1)]$ from Eqs. (2.3), (2.2), (2.7) and (2.8) to the experimental optical data of the InN [14, 15] and TiN [16]. The fitting results of the parameters in Eq. (2.6) are listed in Table 3.1 for indium nitride (InN) and titanium nitride (TiN).



3.2 Dielectric Function and Energy Loss Function

Fig 3.1 shows a comparison on $\epsilon_R(0, \omega)$, $\epsilon_I(0, \omega)$, $\text{Im}[-1/\epsilon(0, \omega)]$ and $\text{Im}[-1/(\epsilon(0, \omega)+1)]$ for InN among the present fittings (solid curves) and the experimental data [14, 15] (dotted curves). It can be seen that the present fittings are in good agreement as compared to the experimental data. The volume and surface excitations exhibit resonant plasmon peaks at around 15 and 13 eV. A similar plot

for TiN is shown in Fig 3.2 among the present fittings (solid curves) and the experimental data [16] (dotted curves). Again, the volume and surface excitations exhibit resonant plasmon main peaks at around 25 and 14 eV. Moreover, we also check the sum rules to assure the correctness of fitting parameters. For the application of finite-range sum rules, we check the calculated effective number of valence electrons at any given energy transfer with the corresponding available optical data. In the case of infinite-range sum rules, we check the accuracy of the total oscillator strength, $\sum_i A_i$. For example, the present fits for InN cover the 4d inner-shell of indium owing to the strong overlapping of oscillator strengths between the valence band and this sub-shell in the proximity of its binding energy. In order to avoid the unclear state in the separation of cross contributions, we extend our fits to higher energy transfers covering these inner-shell excitations.

3.3 Differential Inverse Inelastic Mean Free Path


The differential inverse inelastic mean free paths (DIIMFPs) were calculated for both escaping and incident electrons crossing the surface of InN and TiN using Eqs. (2.23) and (2.24) and the fitted results. The calculated results of the DIIMFP for a 500 eV electron escaping from InN to vacuum with various distances from the surface

crossing point are plotted in Fig. 3.3, either outside ($r > 0$) or inside ($r < 0$) the solid for different crossing angle, α . The DIIMFP for electrons moving inside the solid is approximately independent of crossing angle and distance owing to the compensation of the contributions from volume and surface excitations. For the electrons moving in vacuum, the DIIMFP is entirely contributed from surface excitations. Outside the solid, as the electrons move closer to the surface, corresponding to smaller r values, the DIIMFP becomes larger owing to the increase in surface excitations. Furthermore, the DIIMFP becomes larger for increasing crossing angle at a fixed r value owing to the shorter distance to the surface. Figure. 3.4 shows the calculated results of the DIIMFP for a 500 eV incident electron moving from vacuum to InN with different crossing angles and different distances from the surface crossing point, either outside ($r < 0$) or inside ($r > 0$) the solid. Again, the DIIMFP for incident electrons exhibit similar angular and distance dependences as for escaping electrons. Similar results of the DIIMFP for 500 eV electrons moving between TiN and vacuum are plotted in Figs. 3.5 and 3.6 for the escaping and incident electrons, respectively.

Fig. 3.7 shows the calculated results of the DIIMFP for a 60° crossing angle electron escaping from InN to vacuum for several electron energies with different distances from the surface crossing point. It reveals that the DIIMFP decreases with

increasing electron energy because of the smaller interacting time for volume and surface excitations. However, the plasmon peak remains unchanged. The distance dependence for DIIMFP is the same as we discussed in preceding paragraph. Similar results of the DIIMFP for 60° crossing angle electrons incident from vacuum to TiN are plotted in Fig. 3.8. Again, the DIIMFP for incident electrons exhibit similar energy and distance dependences as for escaping electrons.

3.4 Inverse Inelastic Mean Free Path



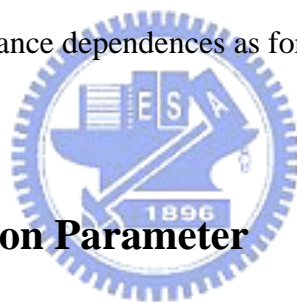
The inverse inelastic mean free paths (inverse IMFPs) were calculated for both escaping and incident electrons crossing the surface of several nitride semiconductors using Eqs. (2.25) and (2.26). The calculated results of the inverse IMFPs with different crossing angles for a 500 eV electron escaping from InN to vacuum are plotted in Fig. 3.9 as a function of electron distances relative to the surface crossing point. When the electrons travel inside the solid ($r < 0$), the inverse IMFP is roughly independent of the crossing angle and the electron distance owing to the approximate compensation of surface and volume excitations. Therefore, the inverse IMFP of the electrons inside the solid approximately equals to the value corresponding to the infinite solid. As the electrons moves outside the solid ($r > 0$),

the inverse IMFP rapidly falls off with the increasing distance from the surface, especially for smaller crossing angles. This indicates that the surface excitations are possible only for electrons near the surface. And the electrons for larger crossing angles are more probable to induce surface excitations owing to these electrons spend longer time near the surface. Fig. 3.10 shows the calculated results of the inverse IMFP for a 500 eV incident electron moving from vacuum to InN with several crossing angles. Again, the inverse IMFP for incident electrons exhibit similar angular and distance dependences as for escaping electrons. However, a comparison between Figs 3.9 and 3.10 indicates that the inverse IMFP for incident electrons in vacuum ($r < 0$) are slightly smaller than that for escaping electrons in vacuum ($r > 0$). This is because the different attractive forces acting on the electrons in vacuum by the surface charges. The force on the incident electrons in vacuum is parallel to the electrons moving direction and hence accelerates the electrons. On the other hand, the force on the escaping electrons in vacuum is anti-parallel to the electrons moving direction and thus decelerates the electron. Consequently, the time spent near the surface for incident electrons in vacuum are less than that for escaping electrons in vacuum, leading to less surface excitations for incident electrons in vacuum. Similar results of the inverse IMFP for 500 eV electrons moving between TiN and vacuum are plotted in Figs. 3.11 and 3.12 for the escaping and incident

electrons, respectively.

Fig. 3.13 shows the calculated results of the inverse IMFP for a 60° crossing angle electron escaping from InN to vacuum with several electron energies. It reveals that the inverse IMFP decreases with increasing electron energy owing to the smaller interacting time volume and surface excitations. The distance dependence for inverse IMFP is the same as we discussed in preceding paragraph. Similar results of the inverse IMFP for 60° crossing angle electrons incident from vacuum to TiN are plotted in Fig. 3.14. Again, the inverse IMFP for incident electrons exhibit similar energy and distance dependences as for escaping electrons.

3.5 Surface Excitation Parameter



The surface excitation parameters (SEPs) were calculated for both escaping and incident electrons of InN and TiN using Eqs. (2.27) and (2.28). The calculated results (solid circles) of the SEPs for electrons escaping moving from InN to vacuum with different electron energies and crossing angles are plotted in Fig. 3.15. It reveals that the SEPs decrease with increasing electron energy due to the smaller interacting time between the electrons and the surface. It can be also seen that the SEPs increase for larger crossing angles due to the longer time for electron-surface

interactions. The SEPs rise slowly with increasing crossing angle until about $\alpha = 70^\circ$, above which such a rise becomes rapidly. Fig 3.16 shows the calculated results (solid circles) of the angular and energy dependent SEPs for incident electrons moving from vacuum to InN. Again, the SEPs for incident electrons exhibit similar energy and angular dependences as for escaping electrons. Here the SEPs of the incident electrons are slightly smaller than that of the escaping electrons due to the electrons acceleration in the former case, as described earlier. The presently calculated SEPs are fitted to Eq. (2.29). The fitting results are also included in Figs. 3.15 and 3.16 as solid curves for comparison. It reveals that the fitting results are in good agreement as compared to the calculated SEPs. Similar results of the SEPs for electrons moving between TiN and the vacuum with different electron energies and crossing angles are plotted in Figs. 3.17 and 3.18 for the escaping and incident electrons, respectively. With E in electron-volts, we list the best fitted values of the parameters a , b and c in Table 3.2 for InN and TiN.

Fig 3.19 is a plot of the SEP for 500 eV electrons escaping from InN to vacuum as a function of the crossing angle. Solid circles, solid curve, dashed curve, and dotted curve are, respectively, the calculated result using Eq. (2.27), the fitting results using Eq. (2.29), the previous model [5], and the Oswald's model [17]. It reveals that the results using previous model work only approximately due to the simplified

$(\cos \alpha)^{-1}$ dependence of the SEP on crossing angle and carrying no restriction on the normal component of momentum transfer in the previous model. There is a large discrepancy between the results present and Oswald's models. The reason is that the Oswald's model is valid only for free-electron-like materials. InN, however, is a semiconductor with small band gap and complex band structure. Fig. 3.20 shows the similar results of the crossing-angle-dependent SEP calculated using Eq. (2.28) for 500 eV electrons incident from vacuum to TiN (solid circles). Again, the results of present fitting (solid curve), the previous model (dashed curve), and the Oswald's model (dotted curve) are included in this figure for comparisons.



CHAPTER 4

Conclusions

InN, a small band gap semiconductor, is an attractive material in the application of laser and light-emitting diodes. TiN, an extremely hard ceramic material, is widely used in protective coatings on cutting tools. In the present work, a modified inelastic-scattering model was applied to calculate the inelastic cross sections for electrons moving across the InN and TiN surface. This model was developed based on the dielectric response theory. The DIIMFP, inverse IMFP, and SEP were calculated using extended Drude dielectric functions with parameters obtained from a fit of this function to the experimental optical data.

It can be seen that the DIIMFP and inverse IMFP for electrons moving inside the solid were roughly independent of the electron distance and crossing angle due to the compensation of surface and volume excitations. Therefore, the inverse IMFP approximately equals to the value corresponding to the infinite solid. When the electrons travel in the vacuum, the DIIMFP and inverse IMFP became larger for increasing crossing angle, or decreasing electron distance owing to the increase in surface excitations. Besides, the DIIMFP and inverse IMFP became smaller for increasing electron energy due to the less interacting time for volume and surface

excitations.

The SEP calculated as the integration of the inverse IMFP over whole path length of the electron in vacuum. Thus the SEP increases with increasing crossing angle or decreasing electron energy. The attractive force on the escaping or incident electron exerted by the surface induced charge decelerates or accelerates the electron, respectively. Therefore, the DIIMFP, inverse IMFP and SEP of escaping electrons in vacuum are larger than those of incident electron. The presently calculated SEP was found to follow a simple formula as a function of electron energy and crossing angle.



References

- [1] S. Tougaard and I. Chorkendorff, *Phys. Rev. B* **35**, 6570 (1987).
- [2] C. J. Tung, Y. F. Chen, C. M. Kwei, and T. L. Chou, *Phys. Rev. B* **49**, 16684 (1994).
- [3] Y. F. Chen, P. Su, C. M. Kwei, and C. J. Tung, *Phys Rev B* **50**, 17547 (1994).
- [4] Y. F. Chen and C. M. Kwei, *Surf. Sci.* **364**, 131 (1996).
- [5] C. M. Kwei, C. Y. Wang, and C. J. Tung, *Surf. Interface Anal.* **26**, 682 (1998).
- [6] R. H. Ritchie, *Phys. Rev.* **106**, 874 (1957).
- [7] Y. F. Chen, *Surf. Sci.* **519**, 115 (2002).
- [8] Y. C. Li, Y. H. Tu, C. M. Kwei, and C. J. Tung, *Surf. Sci.* **589**, 67 (2005).
- [9] C. M. Kwei, Y. C. Li, and C. J. Tung, *Surf. Sci.* **600**, 3690 (2006).
- [10] C. K. Gan and D. J. Srolovitz, *Phys. Rev. B* **74**, 115319 (2006).
- [11] G. W. Shu, P. F. Wu, M. H. Lo, J. L. Shen, T. Y. Lin, H. J. Chang, Y. F. Chen, C. F. Shih, C. A. Chang and N. C. Chen, *Appl. Phys. Lett.* **89**, 131913 (2006).
- [12] M. S. Trtica, B. M. Gaković, and B. B. Radak, *Russ. J. Phys. Chem. A* **81**, 1429 (2007).
- [13] W. Y. Uen, Z. Y. Li, S. M. Lan, T. N Yang, and S. M. Liao, *Thin Solid Films* **516**, 99 (2007).

- [14] Q. Guo, O. Kato, M. Fujiaawa, and A. Yoshida, *Solid State Commun.* **83**, 721 (1992).
- [15] Q. Guo, H. Ogawa, and A. Yoshida, *J. Electron. Spectrosc. Relat. Phenom.* **79**, 9 (1996)
- [16] E. D. Palik (Ed.), *Handbook of Optical Constants of Solids II*, Academic Press, New York (1991)
- [17] R. Oswald, Ph. D. Thesis, Eberhard-Karls-Universität, Tübingen (1992).
- [18] J. Daniels, C. V. Festenberg, H. Raether, and K. Zeppenfeld, *Optical Constants of Solids by Electron Spectroscopy*, Vol. 54 of Springer Tracs in Modern Physics, Springer, New York (1970).
- [19] C. M. Kwei, Y. F. Chen, C. J. Tung, and J. P. Wang, *Surf. Sci.* **293**, 202 (1993).
- [20] D. Y. Smith and E. Shiles, *Phys. Rev. B* **17**, 4689 (1978).
- [21] R. H. Ritchie and A. Howie, *Phyl. Mag.* **36**, 463 (1977).
- [22] R. H. Ritchie, R. N. Hamm, J. E. Turner, H. A. Wright and W. E Bolch., *Physical and Chemical Mechanisms in Molecular Radiation Biology*, Plenum, New York (1991).
- [23] F. Yubero, J. M. Sanz, B. Ramskov and S. Tougaard, *Phys. Rev. B* **53**, 9719 (1996).
- [24] Z. J. Ding, *J. Phys.: Condens. Matter* **10**, 1753 (1998).

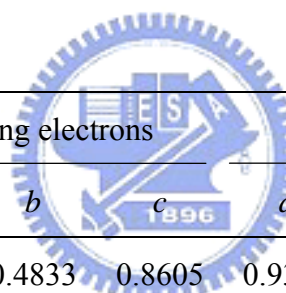
- [25] Y. H. Tu, C. M. Kwei and C. J. Tung, *Surf. Sci.* **601**, 865 (2007).
- [26] C. M. Kwei, S. Y. Chiou and Y. C. Li, *J. Appl. Phys.* **85**, 8247 (1999).
- [27] F. Yubero and S. Tougaard, *Phys. Rev. B* **46**, 2486 (1992).
- [28] F. Flores and F. Garcia-Moliner, *J. Phys. C* **12**, 907 (1979).



Table 3.1 Parameters in the dielectric function of Eq. (2.6) for InN and TiN.

InN ($\epsilon_B=1.2$)			TiN ($\epsilon_B=1$)		
$A_i(\text{eV}^2)$	$\gamma_i(\text{eV})$	$\omega_i(\text{eV})$	$A_i(\text{eV}^2)$	$\gamma_i(\text{eV})$	$\omega_i(\text{eV})$
3.00	1.50	3.00	55.00	0.70	0.10
15.00	5.00	3.50	64.00	3.10	5.00
65.00	2.70	5.40	8.00	2.00	5.40
17.00	1.60	8.00	25.00	2.50	6.50
1.00	1.00	8.50	15.00	4.80	7.40
2.00	1.00	8.90	90.00	4.60	8.80
3.00	1.10	9.00	29.80	3.67	13.30
100.00	4.10	10.30	160.00	10.80	19.80
20.00	4.00	12.60			
56.00	6.00	20.10			
30.00	5.00	27.00			
25.00	4.00	24.00			
28.00	5.00	32.00			
35.00	20.00	36.00			
65.00	10.00	40.00			

Table 3.2 Fitted values of parameters a , b and c in Eq. (2.29) for InN and TiN.



	Escaping electrons			Incident electrons		
	a	b	c	a	b	c
InN	1.8351	0.4833	0.8605	0.9362	0.4862	1.1248
TiN	3.3378	0.5039	0.8292	1.7079	0.5088	1.1040

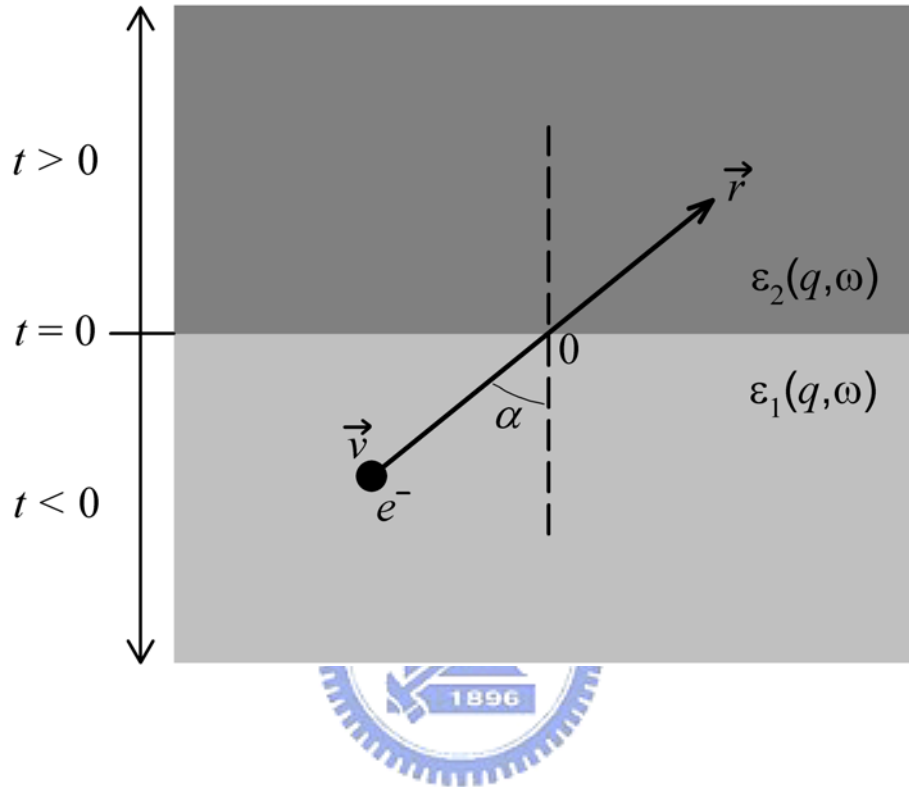


Fig. 2.1 A plot of the problem studied in this work. An electron of charge e^- and velocity \vec{v} moves across the interface at time $t = 0$ from medium 1 to medium 2 with crossing angle α . $\epsilon_1(q, \omega)$ and $\epsilon_2(q, \omega)$ are, respectively, dielectric functions of the media 1 and 2. The instant position of the electron is $\vec{r} = \vec{v}t$, relative to the crossing point at the interface.

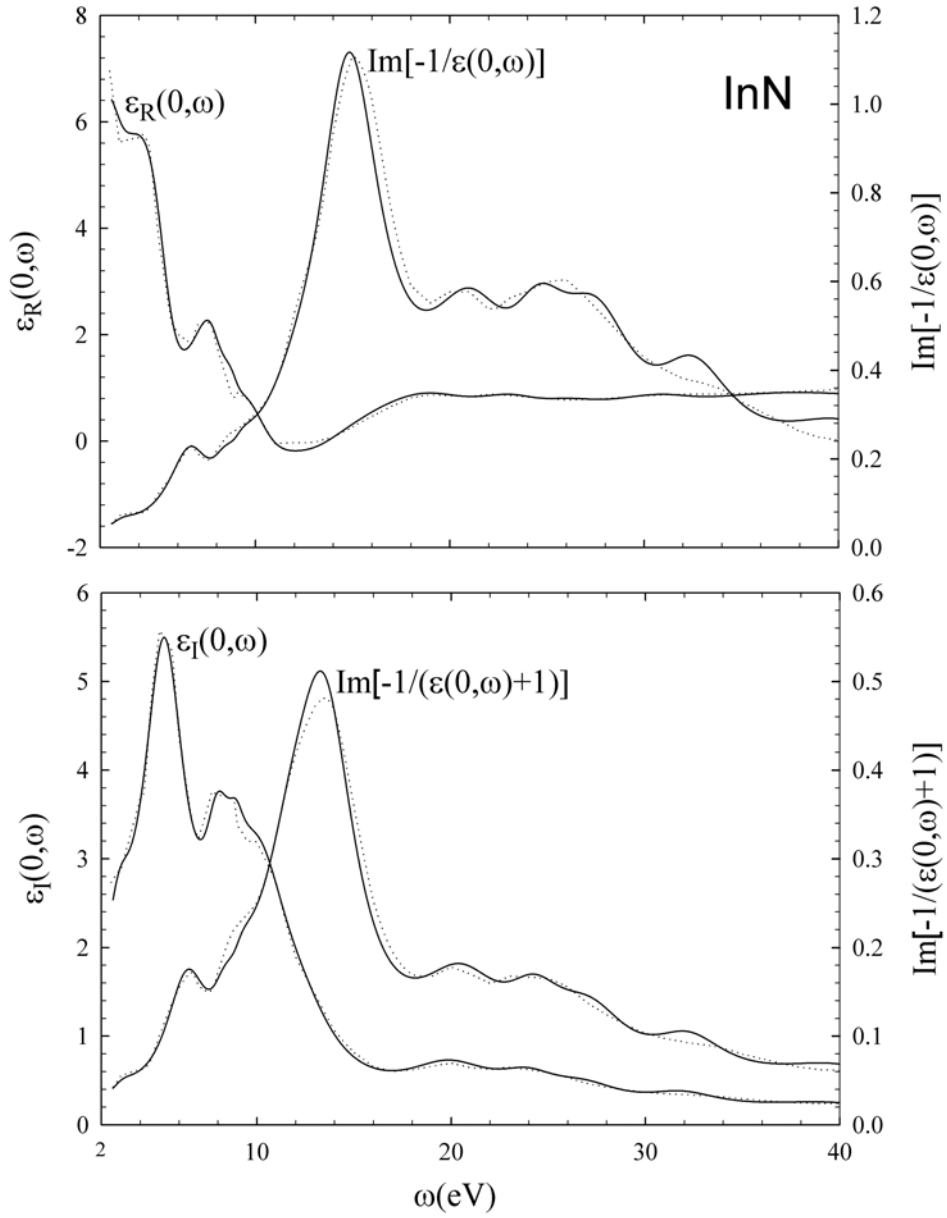


Fig 3.1 A plot of the real and imaginary parts of the dielectric function, $\epsilon_R(0, \omega)$ and $\epsilon_I(0, \omega)$, and the volume and surface loss functions, $\text{Im}[-1/\epsilon(0, \omega)]$ and $\text{Im}[-1/(\epsilon(0, \omega)+1)]$, for InN. Solid and dotted curves are, respectively, calculated results of the present work and experimental data [14, 15].

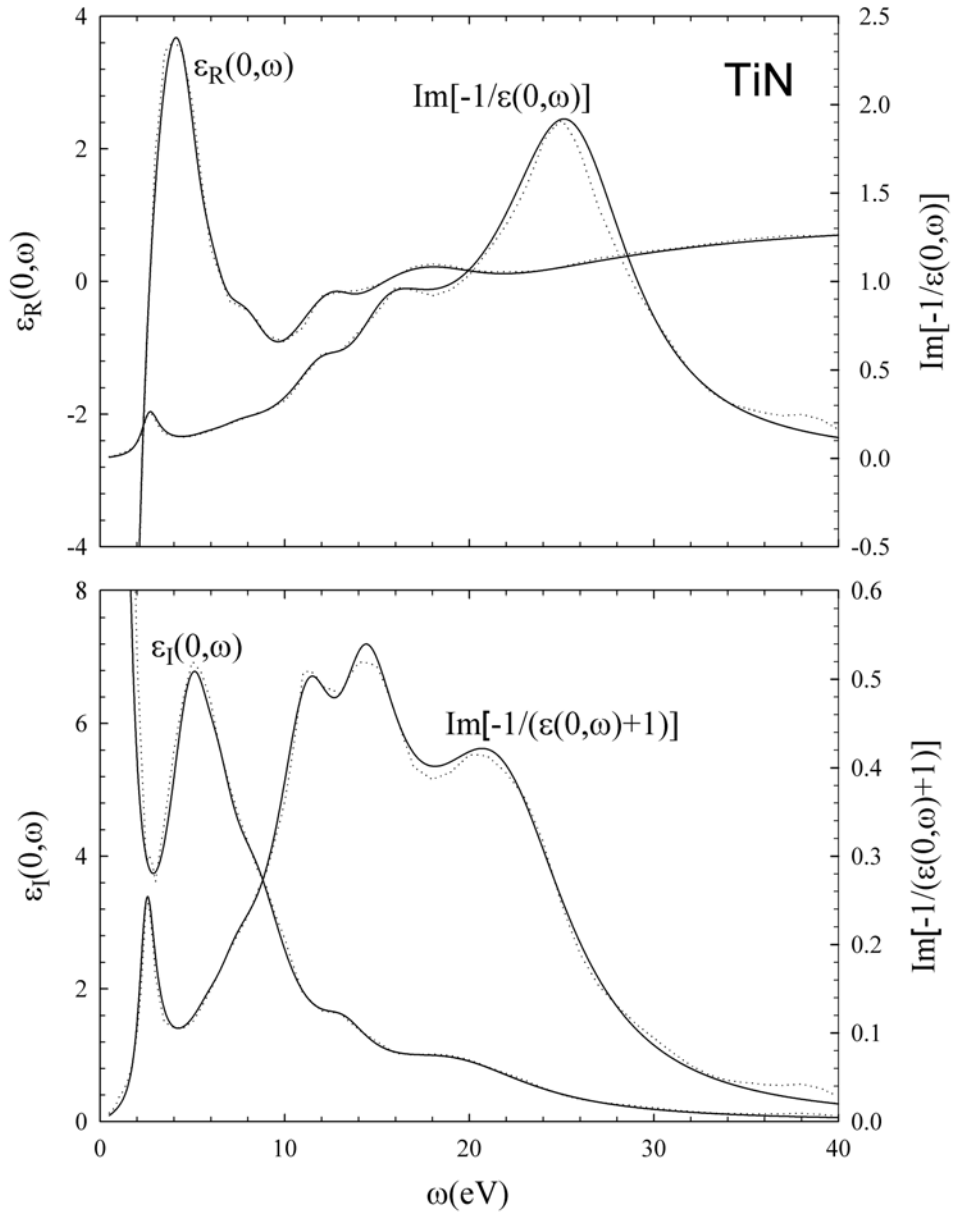


Fig. 3.2 A plot of the real and imaginary parts of the dielectric function, $\epsilon_R(0, \omega)$ and $\epsilon_I(0, \omega)$, and the volume and surface loss functions, $\text{Im}[-1/\epsilon(0, \omega)]$ and $\text{Im}[-1/(\epsilon(0, \omega)+1)]$, for TiN. Solid and dotted curves are, respectively, calculated results of the present work and experimental data [16].

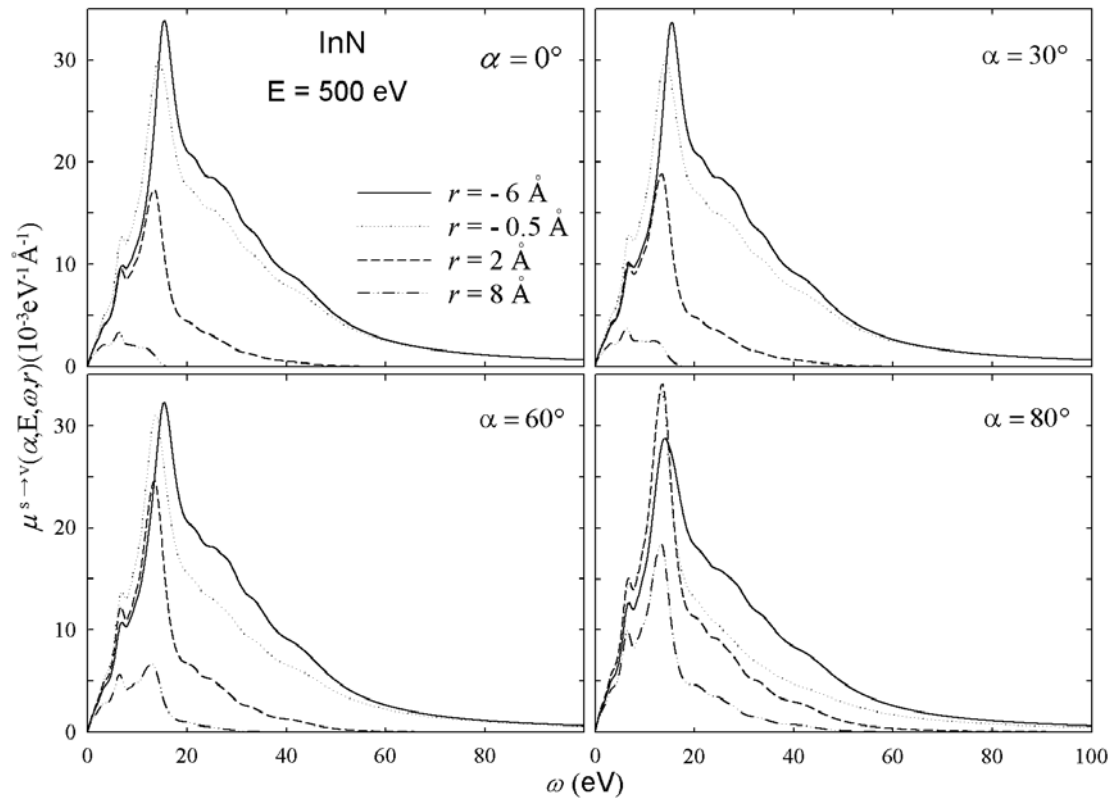


Fig 3.3 Calculated results of the DIIMFP for a 500 eV electron escaping from InN to vacuum with different crossing angles and distances from the crossing point at the surface, either outside ($r > 0$) or inside ($r < 0$) the solid.

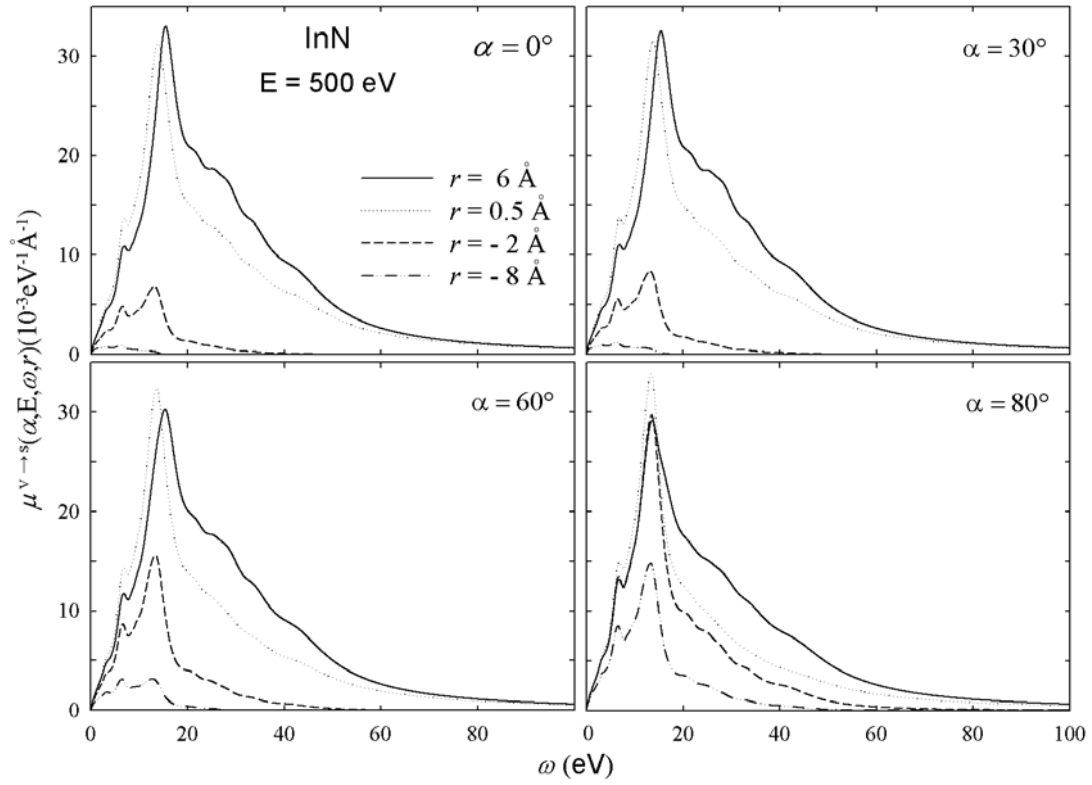


Fig 3.4 Calculated results of the DIIMFP for a 500 eV electron incident from vacuum to InN with different crossing angles and distances from the crossing point at the surface, either outside ($r < 0$) or inside ($r > 0$) the solid.

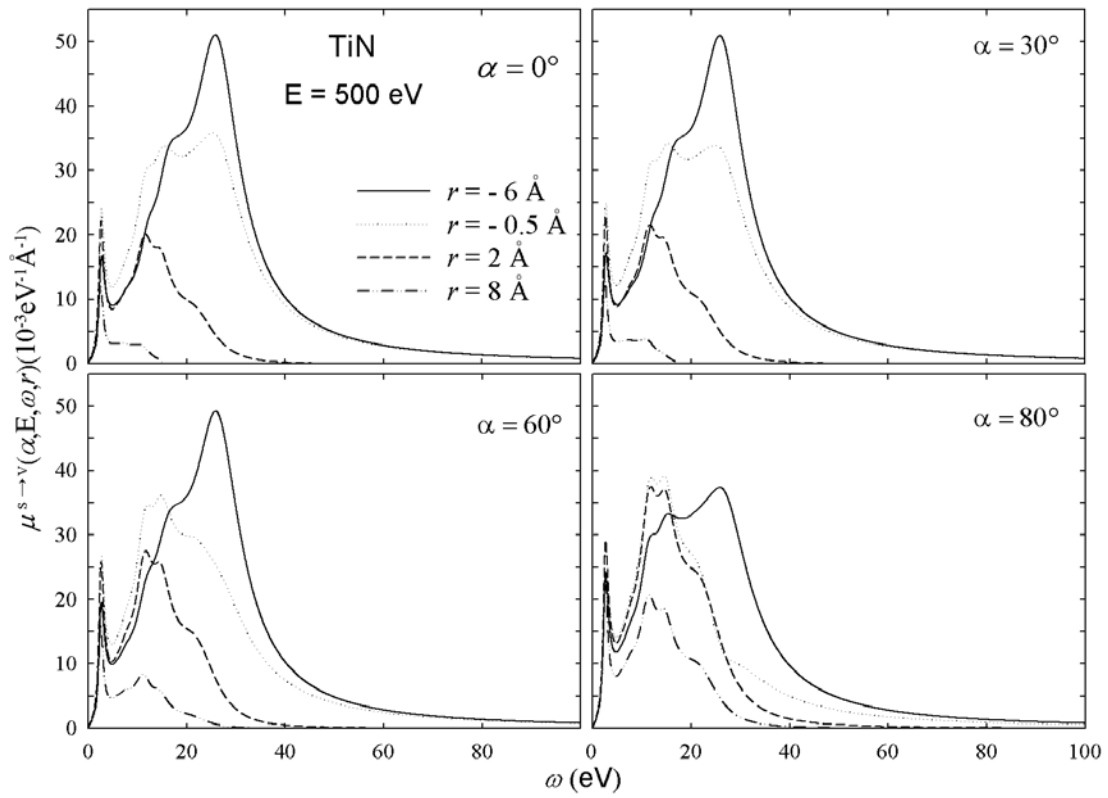


Fig 3.5 Calculated results of the DIIMFP for a 500 eV electron escaping from TiN to vacuum with different crossing angles and distances from the crossing point at the surface, either outside ($r > 0$) or inside ($r < 0$) the solid.

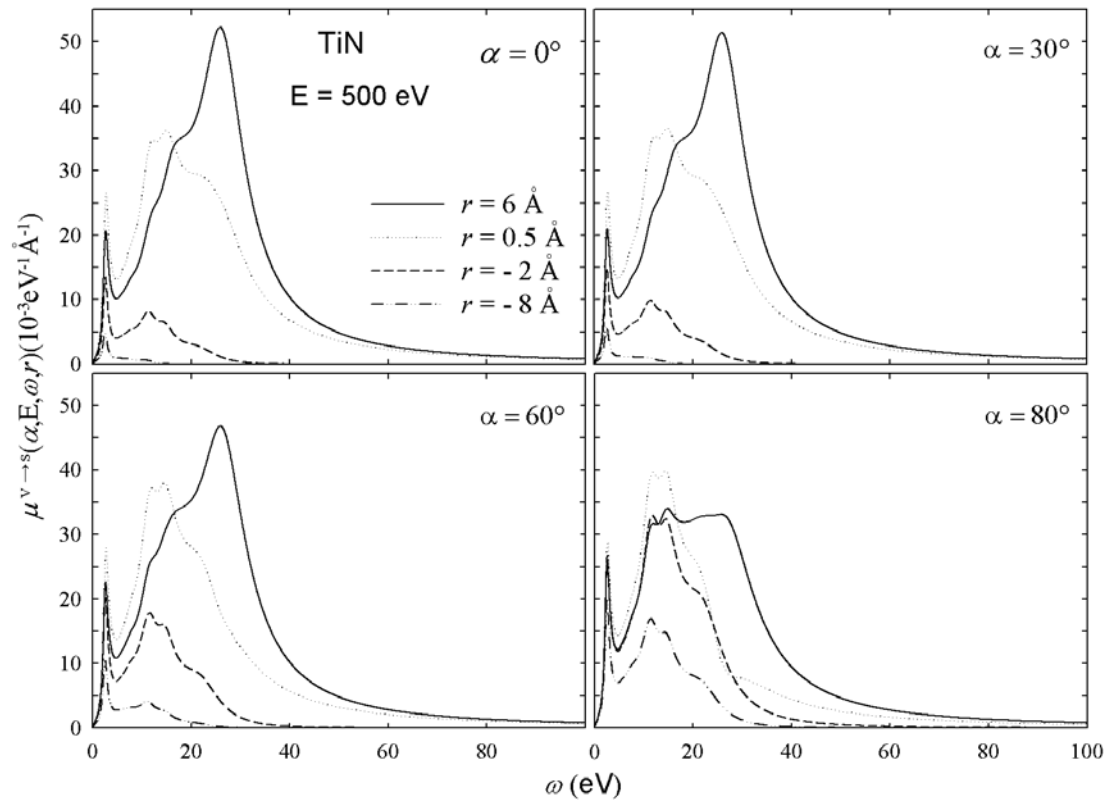


Fig 3.6 Calculated results of the DIIMFP for a 500 eV electron incident from vacuum to TiN with different crossing angles and distances from the crossing point at the surface, either outside ($r < 0$) or inside ($r > 0$) the solid.

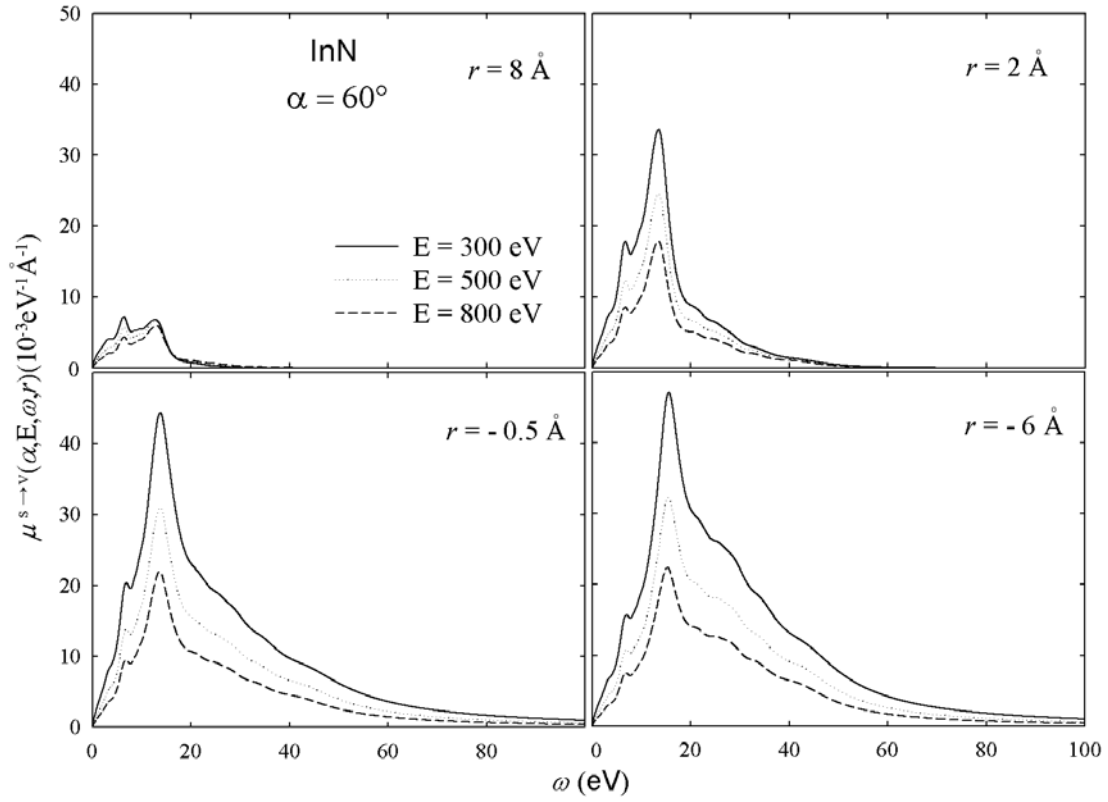


Fig 3.7 Calculated results of the DIIMFP for a 60° crossing angle electron escaping from InN to vacuum for several electron energies with different distances from the crossing point at the surface, either outside ($r > 0$) or inside ($r < 0$) the solid.

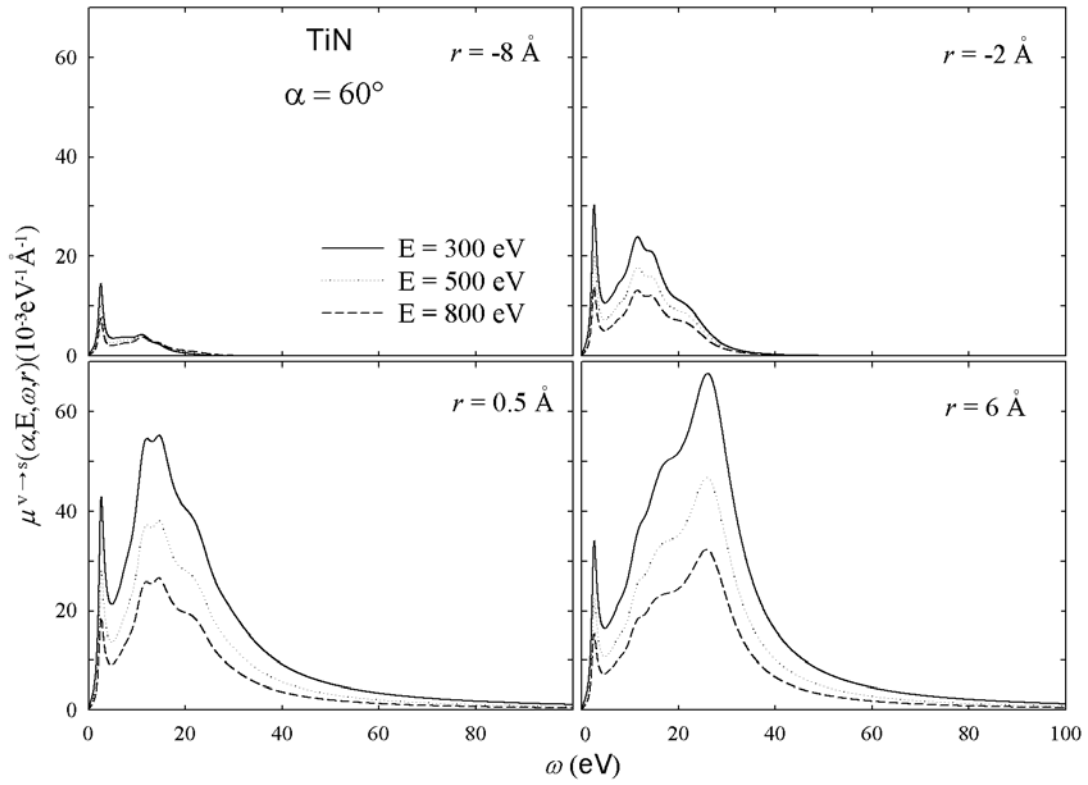


Fig 3.8 Calculated results of the DIIMFP for a 60° crossing angle electron incident from vacuum to TiN for several electron energies with different distances from the crossing point at the surface, either outside ($r < 0$) or inside ($r > 0$) the solid.

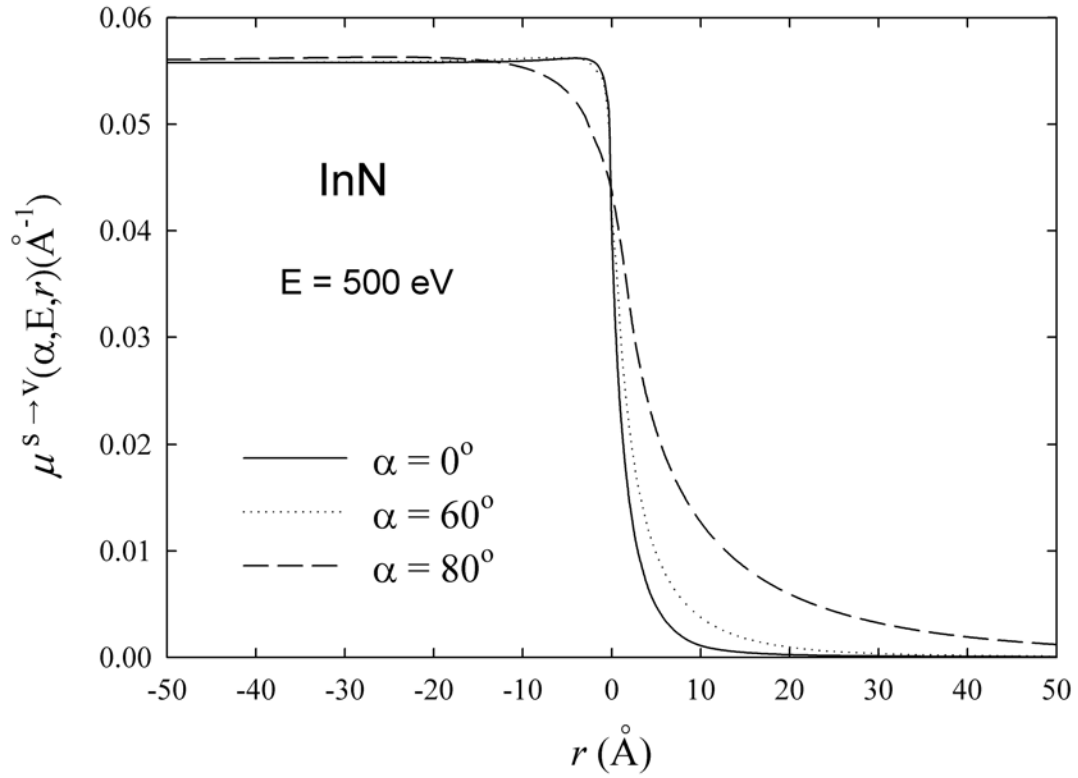


Fig 3.9 A plot of the inverse IMFP for a 500 eV electron escaping from InN to vacuum with different crossing angles as a function of electron distance from the crossing point at the surface, either outside ($r > 0$) or inside ($r < 0$) the solid.

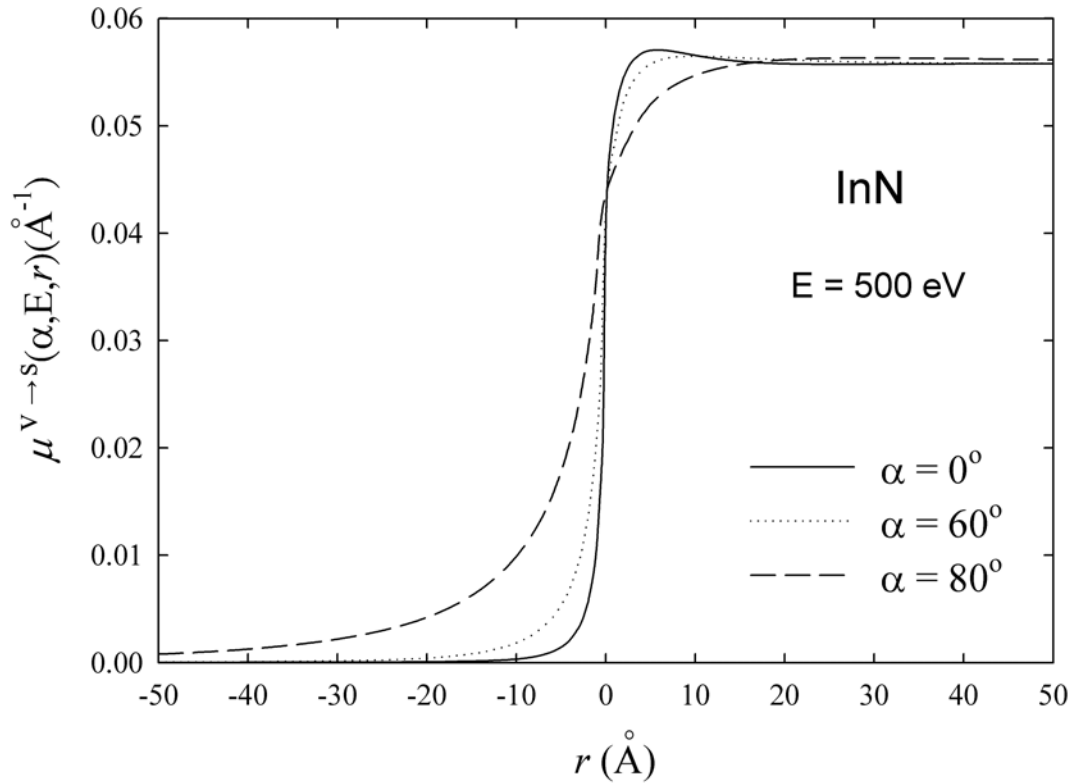


Fig 3.10 A plot of the inverse IMFP for a 500 eV electron incident from vacuum to InN with different crossing angles as a function of electron distance from the crossing point at the surface, either outside ($r < 0$) or inside ($r > 0$) the solid.

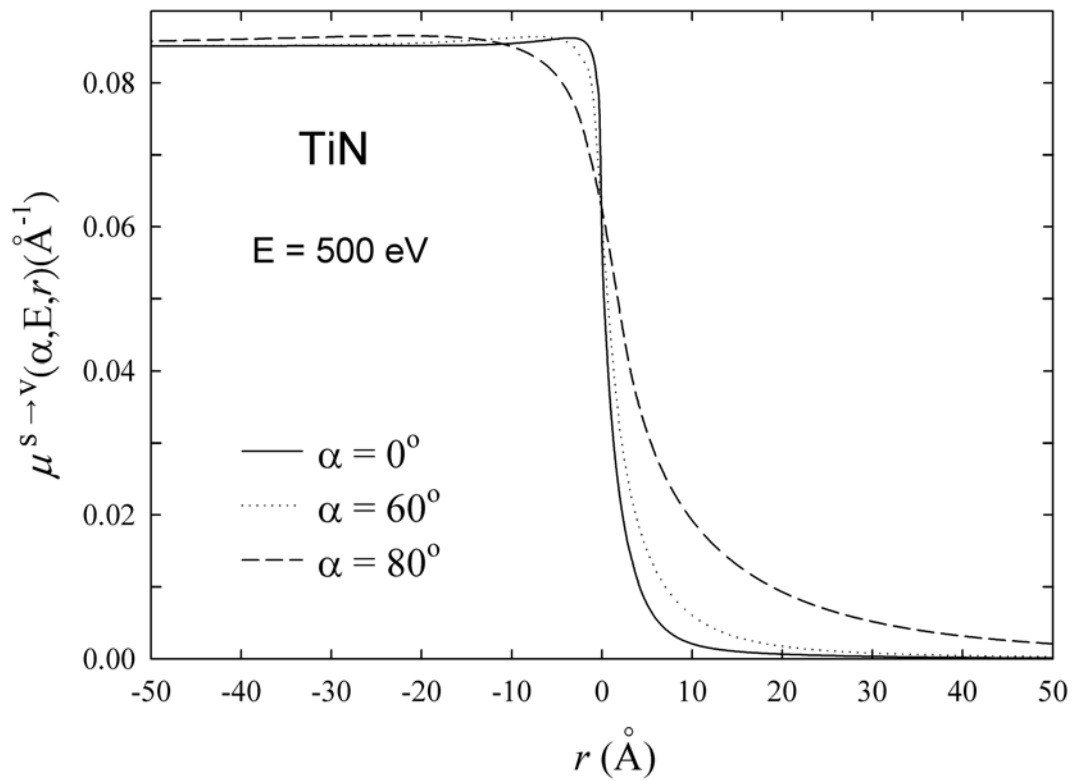


Fig 3.11 A plot of the inverse IMFP for a 500 eV electron escaping from TiN to vacuum with different crossing angles as a function of electron distance from the crossing point at the surface, either outside ($r > 0$) or inside ($r < 0$) the solid.

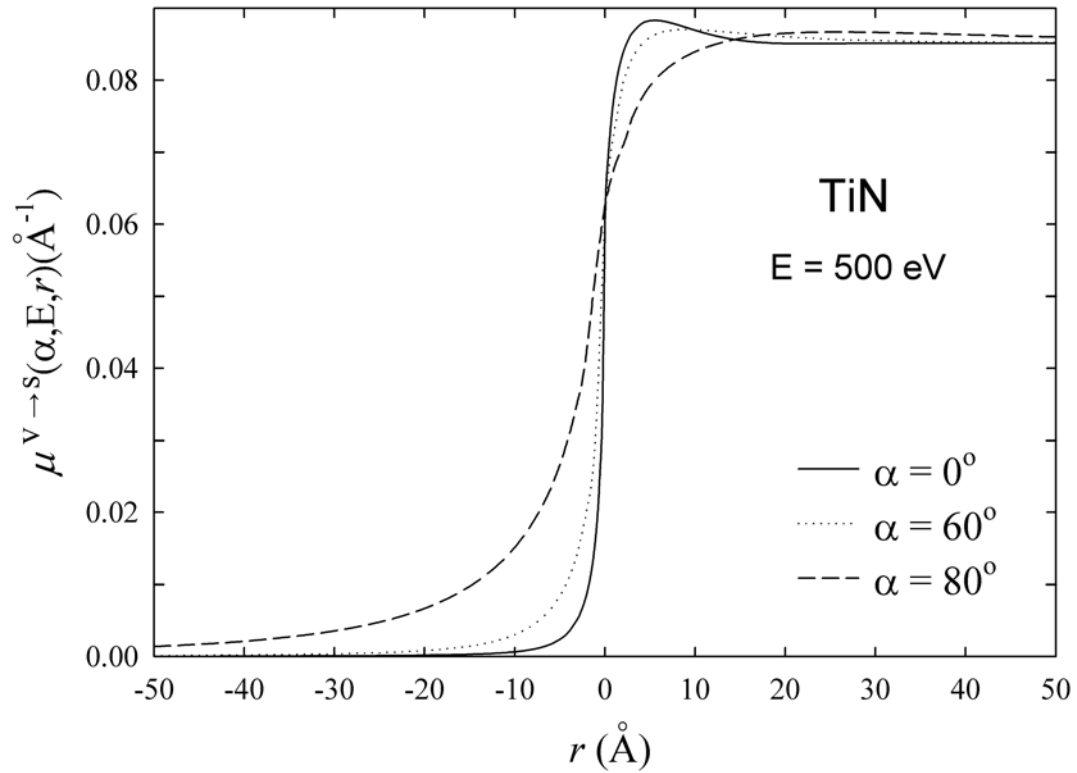


Fig 3.12 A plot of the inverse IMFP for a 500 eV electron incident from vacuum to TiN with different crossing angles as a function of electron distance from the crossing point at the surface, either outside ($r < 0$) or inside ($r > 0$) the solid.

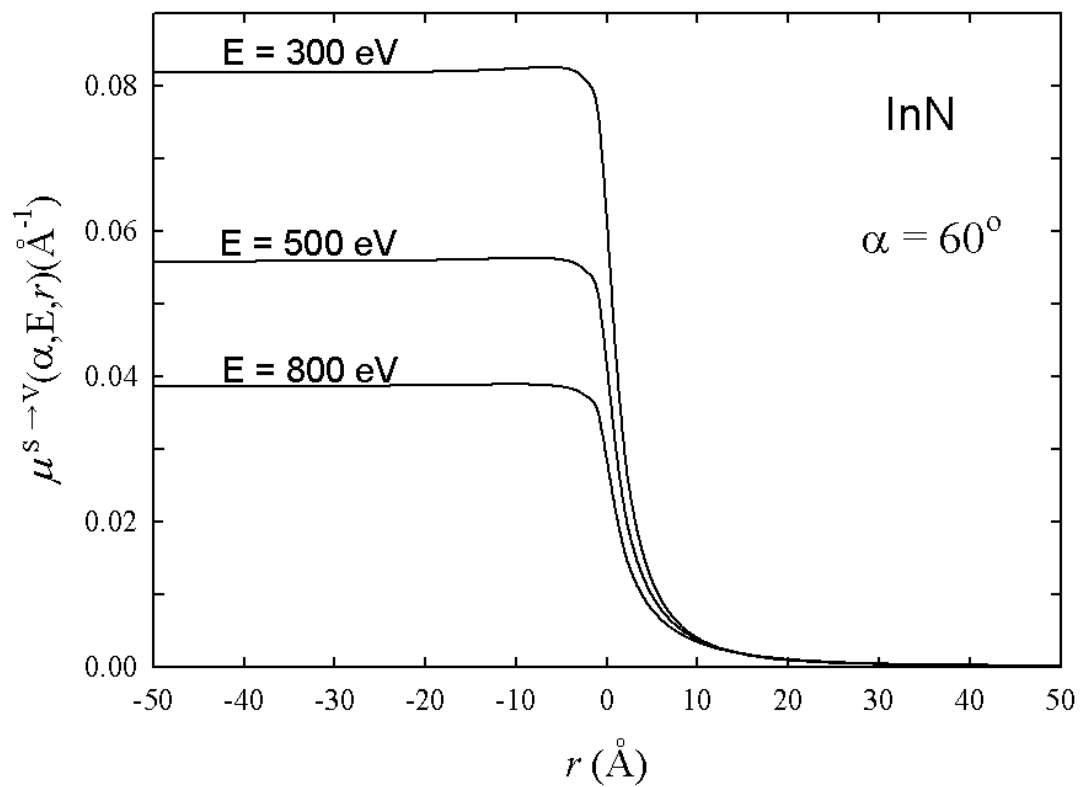


Fig 3.13 A plot of the inverse IMFP for a 60° crossing angle electron escaping from InN to vacuum with different electron energies as a function of electron distance from the crossing point at the surface, either outside ($r > 0$) or inside ($r < 0$) the solid.

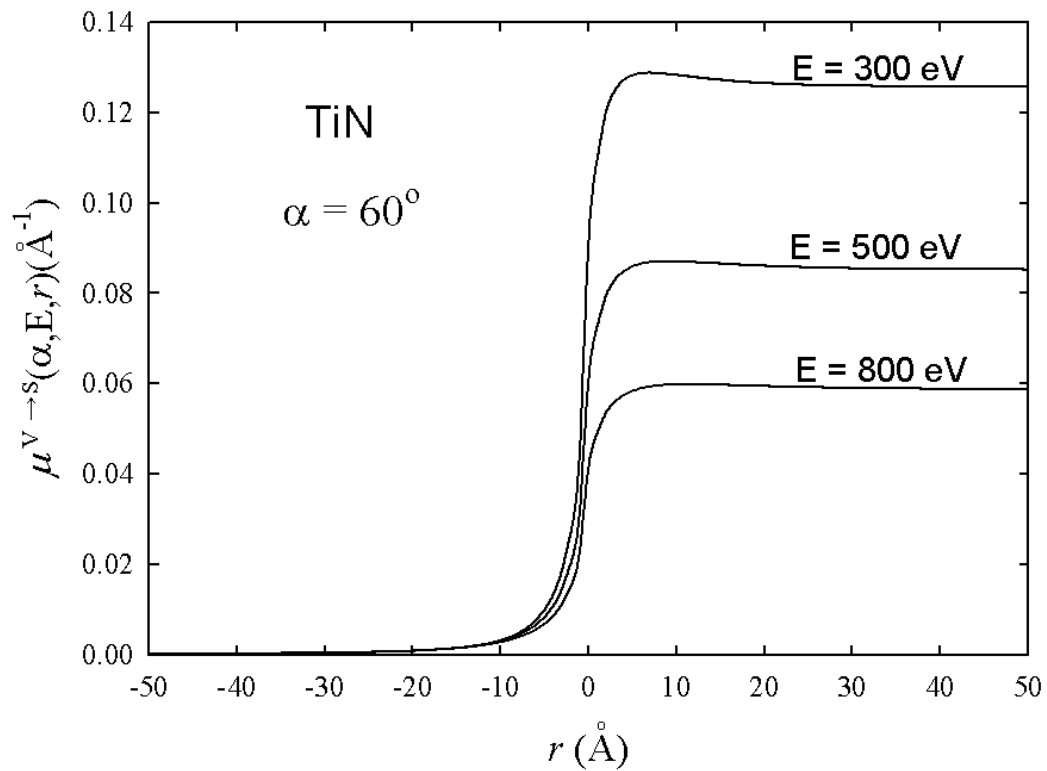


Fig 3.14 A plot of the inverse IMFP for a 60° crossing angle electron incident from vacuum to TiN with different electron energies as a function of electron distance from the crossing point at the surface, either outside ($r < 0$) or inside ($r > 0$) the solid.

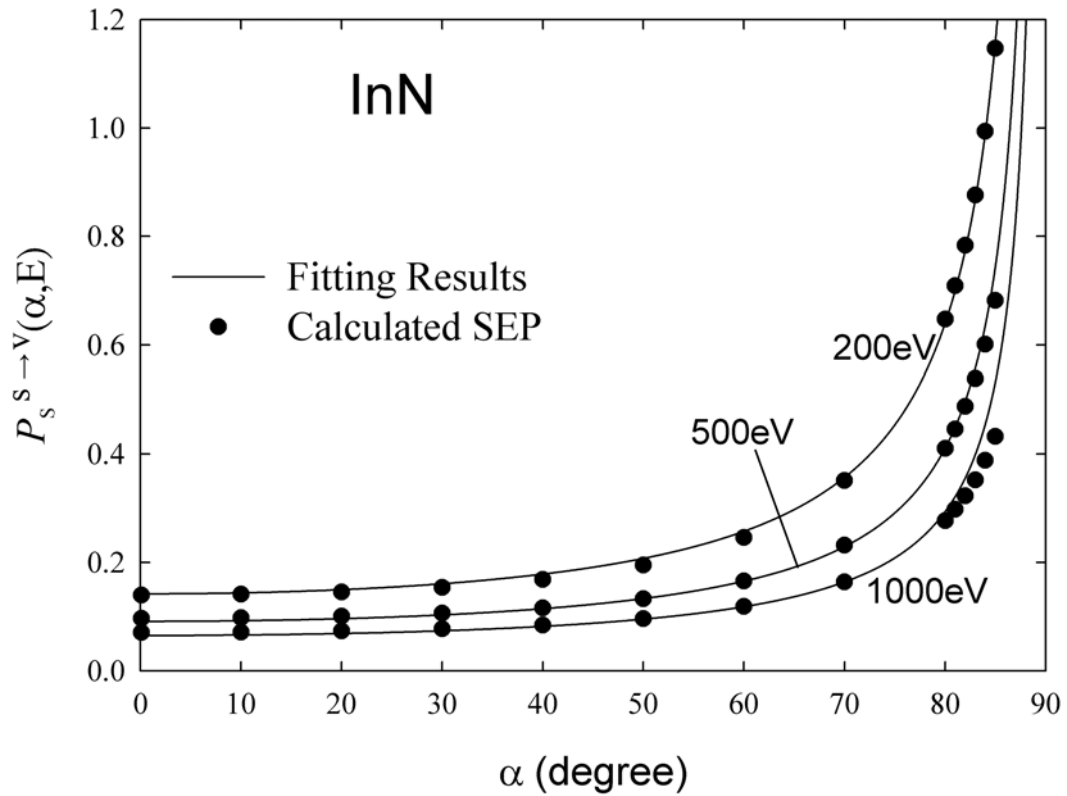


Fig. 3.15 A plot of the SEP for escaping electrons from InN to vacuum as a function of electron energy and crossing angle. Solid circles are the calculated results using Eq. (2.27). Solid curves are the fitting results using Eq. (2.29).

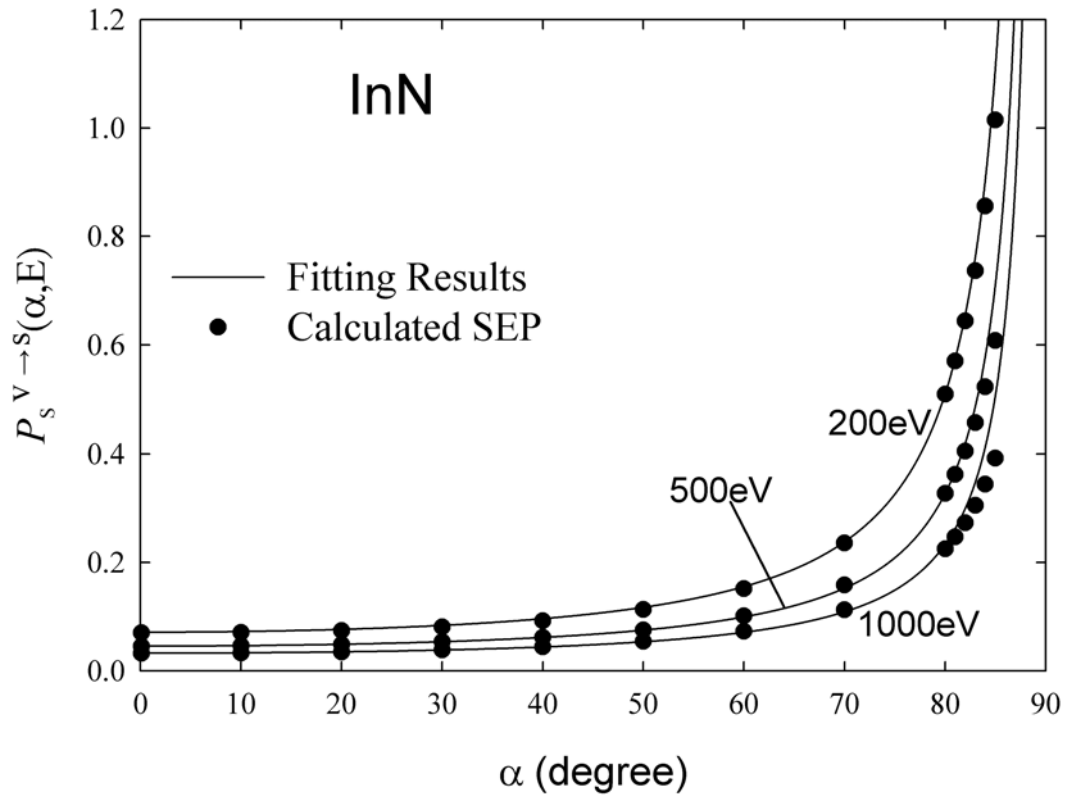


Fig. 3.16 A plot of the SEP for incident electrons from vacuum to InN as a function of electron energy and crossing angle. Solid circles are the calculated results using Eq. (2.28). Solid curves are the fitting results using Eq. (2.29).

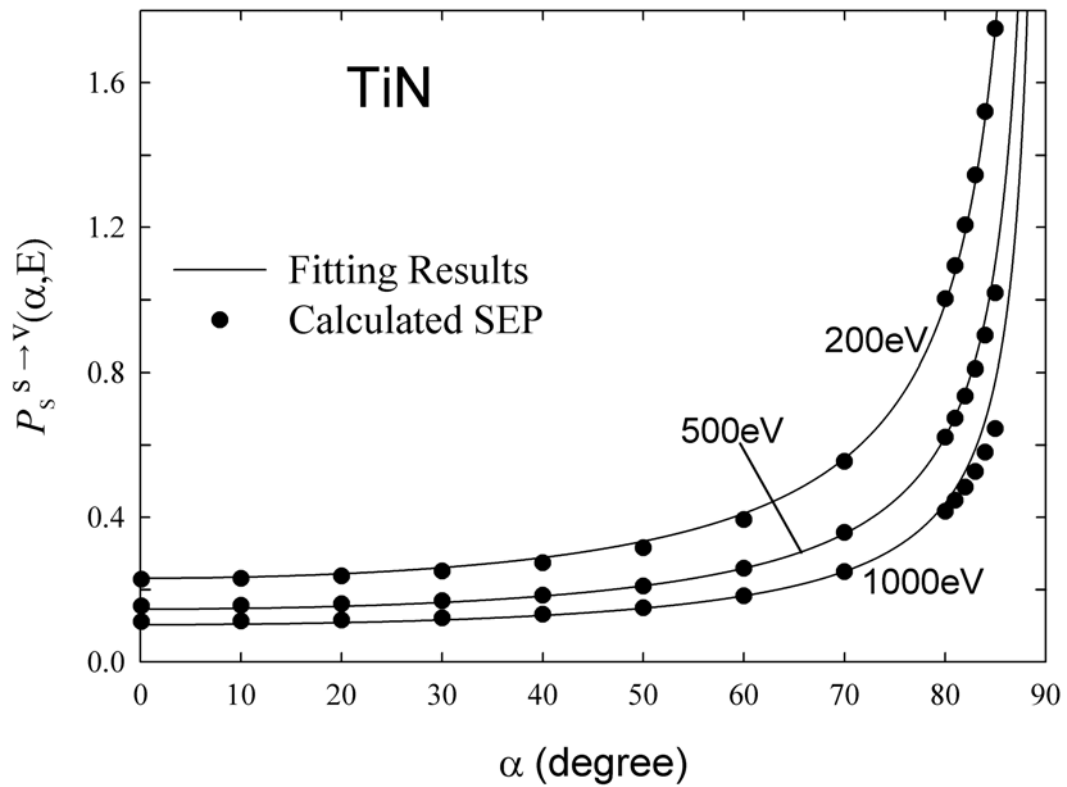


Fig. 3.17 A plot of the SEP for escaping electrons from TiN to vacuum as a function of electron energy and crossing angle. Solid circles are the calculated results using Eq. (2.27). Solid curves are the fitting results using Eq. (2.29).

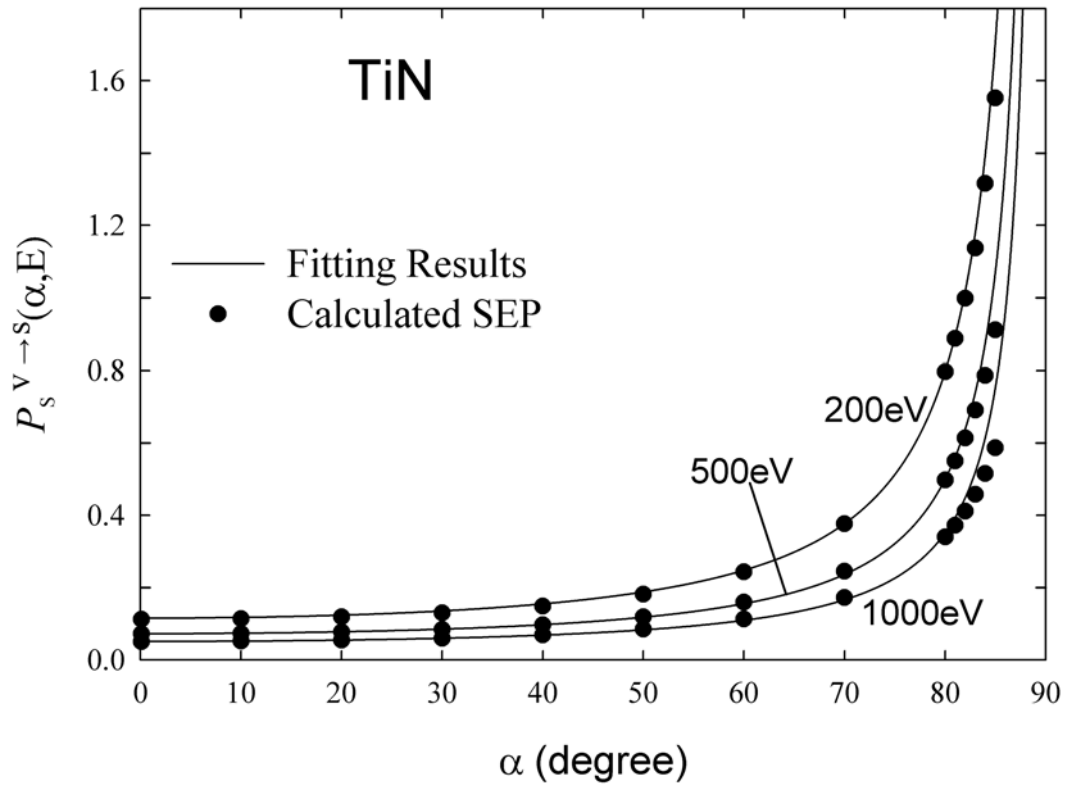


Fig. 3.18 A plot of the SEP for incident electrons from vacuum to TiN as a function of electron energy and crossing angle. Solid circles are the calculated results using Eq. (2.28). Solid curves are the fitting results using Eq. (2.29).

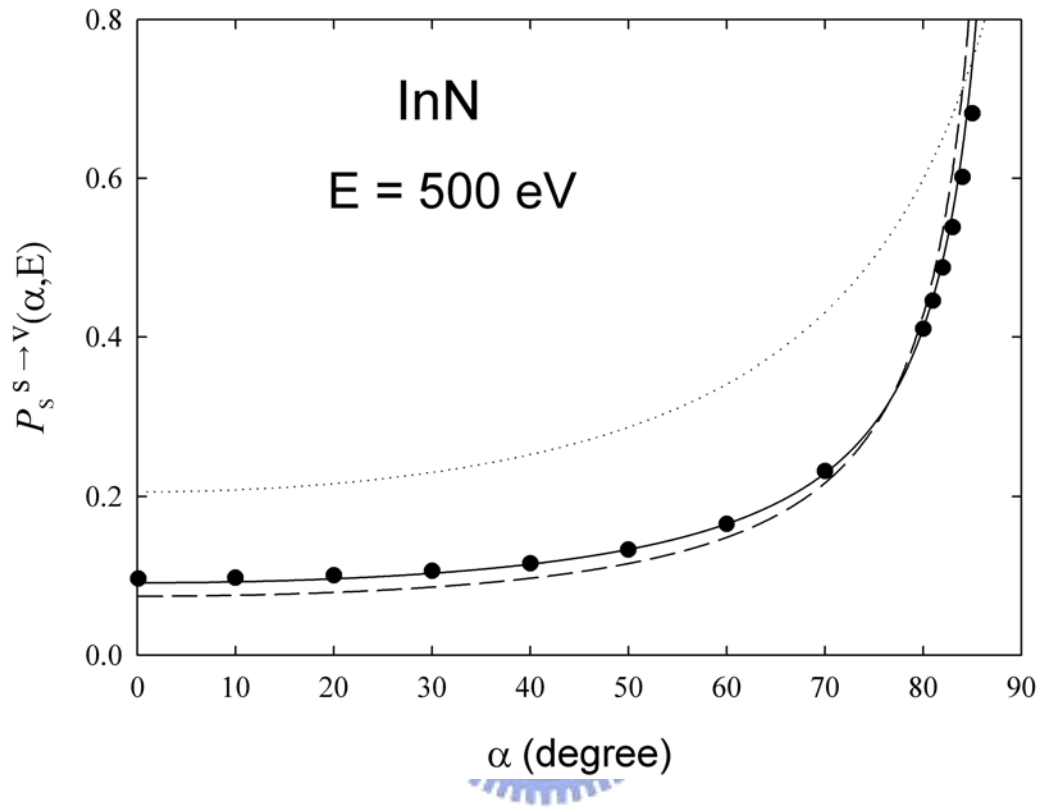


Fig. 3.19 A plot of the SEP for 500 eV electrons escaping from InN to vacuum as a function of the crossing angle. Solid circles, solid curve, dashed curve, and dotted curve are, respectively, the calculated result using Eq. (2.27), the fitting results using Eq. (2.29), the previous model [5], and the Oswald's model [17].

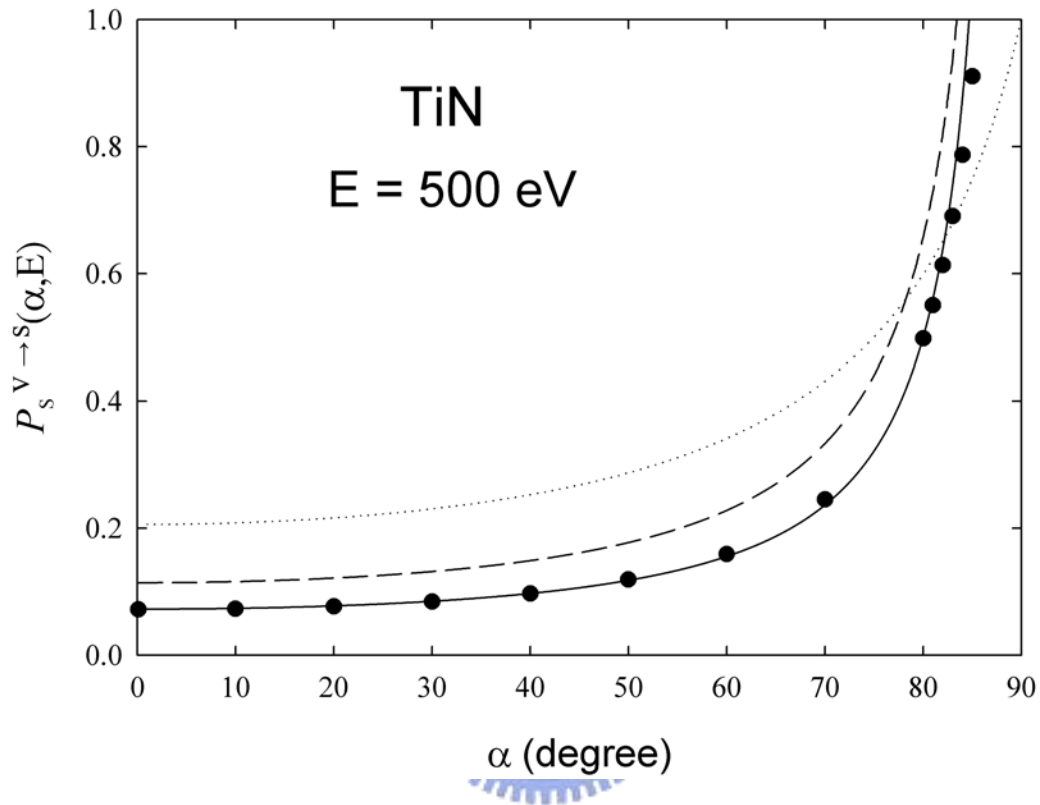


Fig. 3.20 A plot of the SEP for 500 eV electrons incident from vacuum to TiN as a function of the crossing angle. Solid circles, solid curve, dashed curve, and dotted curve are, respectively, the calculated result using Eq. (2.28), the fitting results using Eq. (2.29), the previous model [5], and the Oswald's model [17].

簡 歷

姓 名：姜崇勝

性 別：男

學 歷：

國立彰化師範大學電機工程學系（90年9月～94年6月）

國立交通大學電子研究所碩士班（95年9月～97年6月）

